University of Crete
Department of Physics

Bachelor Diploma Thesis

Airy beams and their peculiar propagation dynamics

Emmanouil Theodoros Kokkinakis

Supervisor: Dimitris Papazoglou, Associate Professor,
Department of Materials Science and Technology,
University of Crete

Committee members:

Kostantinos Makris, Assistant Professor,
Physics Department, University of Crete

George Kopidakis, Associate Professor,
Department of Materials Science and Technology,
University of Crete

Heraklion, June 2022

Abstract

Recently, Airy beams, a new kind of non-spreading optical beams where the amplitude distribution is described by an Airy function, have been introduced. In contrast to other non-spreading optical waves the Airy distribution is the only dispersion-free solution in one dimension. Likewise, Airy beams are also referred to as "accelerating" since they propagate in a curved trajectory, like that of a projectile moving under the action of gravity. Furthermore, they are able to self-heal and bypass obstacles. These novel properties make them exciting for applications.

In this thesis we numerically study the propagation dynamics of 1D Airy beams. We compare our results with analytic or empirical solutions that have been presented in the bibliography. Likewise, by varying the initial conditions we demonstrate the ballistic dynamics of the Airy beam trajectory and by applying obstacles we study their self-healing properties. Finally, we study the autofocusing character of a complex wave that is comprised by two counterpropagating Airy beams and demonstrate the Janus wave signature by focusing such waves using a lens.

Περίληψη

Πρόσφατα παρουσιάστηκαν οι δέσμες *Airy*, ένα νέο είδος μη περιθλώμενων οπτικών δεσμών, των οποίων η κατανομή πλάτους περιγράφεται από μια συνάρτηση *Airy*. Σε αντίθεση με άλλα κύματα φωτός που δεν περιθλώνται, η κατανομή *Airy* είναι η μόνη μη περιθλώμενη λύση της παραξονικής κυματικής εξίσωσης σε μία διάσταση. Επίσης, οι δέσμες *Airy* αναφέρονται και ως ¨επιταχυνόμενες¨, καθώς διαδίδονται σε παραβολική τροχιά, όπως αυτή ενός βλήματος που κινείται υπό την επίδραση της βαρύτητας. Επιπλέον, είναι σε θέση να αυτοαναδομούνται και να παρακάμπτουν τα εμπόδια. Αυτές οι νέες ιδιότητες τις καθιστούν συναρπαστικές για εφαρμογές.

Σε αυτή την εργασία μελετάμε αριθμητικά τη δυναμική διάδοσης μονοδιάστα-των δεσμών *Airy*. Συγκρίνουμε τα αποτελέσματά μας με αναλυτικές ή εμπειρικές λύσεις που έχουν παρουσιαστεί στη βιβλιογραφία. Ομοίως, μεταβάλλοντας τις αρχικές συνθήκες αποδεικνύουμε τη βαλλιστική δυναμική της τροχιάς της δέσμης *Airy* και εφαρμόζοντας εμπόδια μελετάμε τις αυτοθεραπευτικές τους ιδιότητες. Τέλος, μελετάμε τον χαρακτήρα αυτοεστίασης ενός σύνθετου κύματος που απο-τελείται από δύο αντίθετα διαδιδόμενες δέσμες *Airy* και αναδεικνύουμε την υπο-γραφή του κύματος *Janus* μέσω εστίασης τέτοιων κυμάτων με τη χρήση φακού.

Acknowledgements

I would first like to express my heartfelt gratitude to my supervisor, Dimitris Papazoglou, for the invaluable help that he offered me during this semester for the preparation of this thesis, always with consistency, patience and sincere interest. He generously gave me the opportunity to conduct this thesis, at a difficult point in my student career, introducing me to the fascinating field of Optics in the most enjoyable way. I express my thanks, therefore, to an outstanding scientist and teacher, but above all to a man of rare quality.

Also, I would like to thank my family, my mother Maria and my father Antonis, who have been unceasingly by my side all these years and have supported me in all my choices, even the difficult ones. I owe a special thanks to my father, now a colleague, who passed on to me his love for the science of Physics. My gratitude to you both cannot be expressed in a few lines.

Of course, I want to say a huge thank you to my girlfriend, Angelina, for her constant support throughout this time, helping me with patience to overcome every obstacle.

Finally, I would like to thank my friends, whose support during this period has been priceless.

Contents

Chapter 1

Wave propagation and non-diffracting beams

1.1 Helmholtz Equation

As it is known from classical electrodynamics, the electric field $\vec{E}(\vec{r}, t)$ of an electromagnetic wave in vacuum is solution of the wave equation, i.e

$$\nabla^2 \vec{E}(\vec{r}, t) - \frac{1}{c^2} \frac{\partial^2 \vec{E}(\vec{r}, t)}{\partial t^2} = 0 \tag{1.1}$$

where $c = \frac{1}{\sqrt{\mu_0 \epsilon_0}}$ is the speed of light in vacuum and μ_0, ϵ_0 are the vacuum permeability and permittivity, respectively. Choosing a unit polarization vector $\hat{n}$ in a plane perpendicular to the propagation axis, we can express $\vec{E}(\vec{r}, t)$ as $\vec{E}(\vec{r}, t) = E(\vec{r}, t)\ \hat{n}$. It is obvious that $E(\vec{r}, t)$ satisfies the wave equation (1.1).

Separating variables for the electric field, i.e $E(\vec{r}, t) = A(\vec{r}) \cdot T(t)$, and substituting in (1.1), we obtain:

$$\frac{\nabla^2 A}{A} = \frac{1}{c^2 T} \frac{\partial^2 T}{\partial t^2} = -k^2 \tag{1.2}$$

which leads us to the following two ordinary differential equations:

$$\frac{\partial^2 T}{\partial t^2} + k^2 c^2 = 0 \tag{1.3}$$

$$(\nabla^2 + k^2) A(\vec{r}) = 0 \tag{1.4}$$

Equation (1.4) is the well known **Helmholtz equation** [1].

Knowing that e^{-ikct} is a solution of (1.3), we may express the electric field $E(\vec{r}, t)$ as $E(\vec{r}, t) = A(\vec{r}) \cdot e^{-ikct}$, describing an electromagnetic wave that travels from left to right.

1.2 Paraxial wave equation

Let's assume that an electromagnetic wave is propagating along z axis and describe its spatial part $A(\vec{r})$ as a carrier wave with a slowly changing amplitude $u(\vec{r})$:

$$A(\vec{r}) = u(\vec{r}) \cdot e^{ikz} \tag{1.5}$$

If we replace (1.5) to the Helmholtz equation (1.4) we obtain:

$$(\nabla_\perp^2 + \frac{\partial^2}{\partial z^2})(u(\vec{r}) \cdot e^{ikz}) + k^2(u(\vec{r}) \cdot e^{ikz}) = 0 \tag{1.6}$$

where with $\nabla_\perp^2$ we denote the transverse part of the Laplacian operator, i.e $\nabla_\perp^2 = \frac{\partial^2}{\partial x^2} + \frac{\partial^2}{\partial y^2}$. After some calculations this equation ends in:

$$\nabla_\perp^2 u(\vec{r}) + \frac{\partial^2 u(\vec{r})}{\partial z^2} + 2ik \cdot \frac{\partial u(\vec{r})}{\partial z} = 0 \tag{1.7}$$

The previous equation (1.7) can be further simplified if we work on the *paraxial regime*. Generally, in geometrical optics, a ray is characterized as *paraxial ray*, when it makes a small angle($\theta \ll 0.1°$) to the optical axis of the system, so that we can assume that $\sin\theta \simeq \tan\theta \simeq \theta$. In our case, this *paraxial approximation*, is translated to the condition that the amplitude $u(\vec{r})$ has a first derivative that is slowly varying function of z. This condition, often also referred as *slowly varying envelope approximation*, is mathematically expressed as:

$$\left|\frac{\partial^2 u(\vec{r})}{\partial z^2}\right| \ll \left|k \cdot \frac{\partial u(\vec{r})}{\partial z}\right| \tag{1.8}$$

After this simplification, we finally get the following relation:

$$i\,\frac{\partial u(\vec{r})}{\partial z} = -\frac{1}{2k}\nabla_\perp^2 u(\vec{r}) \tag{1.9}$$

which is referred as the ***paraxial wave equation***. This result is unexpectedly interesting, since it allows us to make a connection between *wave optics* and *quantum mechanics*. It is obvious that the paraxial wave equation is the *optical analogue* of *Schrödinger's equation* of a free particle:

$$i\hbar \cdot \frac{\partial \psi}{\partial t} = -\frac{\hbar^2}{2m}\nabla^2 \psi \tag{1.10}$$

since the two equations (1.9) and (1.10) are mathematically equivalent, with the obvious correspondences: $z \leftrightarrow t$ and $k \leftrightarrow m/\hbar$.

This analogy is of special interest, and is numerically studied in the Appendix.

1.3 Diffracting and non-diffracting Beams

In general, electromagnetic waves that propagate in free space exhibit the phenomenon of *diffraction*. That means that their spatial field distribution spreads while their propagate so that their maxima's intensity drop. As an example, a solution of the paraxial wave equation (1.9) is the well known *Gaussian beam* where the cylindrically symmetric field distribution as the beam propagates along the z direction,is described by:

$$u(x,y,z) = u_0 \frac{w_0}{w(z)} \cdot e^{-\frac{x^2+y^2}{w^2(z)}} \cdot e^{\frac{ik(x^2+y^2)}{2R(z)}} \cdot e^{-i\phi(z)} \tag{1.11}$$

w_0^2 where $w(z) = w_0\sqrt{1 + \frac{z^2}{z_R^2}}$, $w_0 \equiv w(0)$ is the *beam waist*, $R(z) = z\left(1 + \frac{z_R^2}{z^2}\right)$ is the wavefront *radius of curvature*, $\phi(z) = arctan(z/z_R)$ is the so called *Gouy phase* and $z_R \equiv \pi w^2/\lambda$ is the *Rayleigh range* of the beam.

The intensity of this beam's maximum $I_{max}(z) \equiv I(0,0,z) \propto |u(0,0,z)|^2$ drops while the beam propagates along z axis. We can easily calculate that:

$$\frac{I_{max}(z = z_R)}{I_{max}(z = 0)} = \frac{w^2(0)}{w^2(z_R)} = \frac{1}{2} \tag{1.12}$$

The previous result means that the beam's maximum intensity has dropped to the half of its initial value when propagating for distance $z = z_R$.
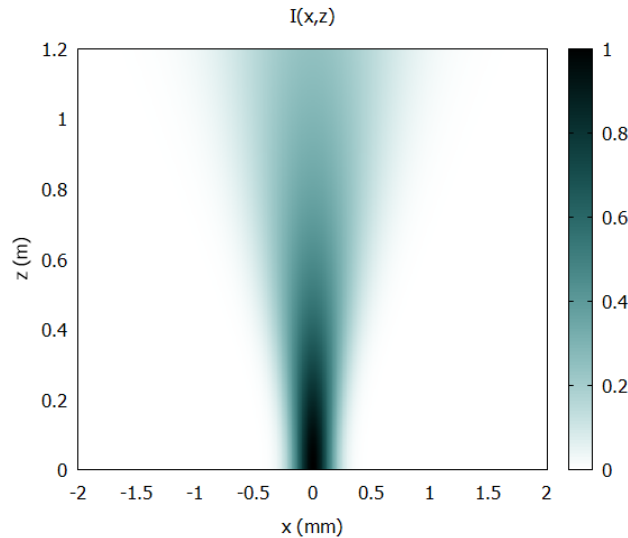

Figure 1.1: Numerical simulation results of the intensity $I(x, z)$ distribution of an 1D Gaussian Beam with wavelength $\lambda = 700$ nm and initial electric field FWHM $w_g = 400\mu$m

It is though possible to find solutions of the paraxial wave equation (1.9) that *do not exhibit diffraction*. Although plane waves are non-diffracting, it's not feasible to generate them since they would contain infinite energy. In 1987, Durnin et al [2], [3] firstly succeeded to theoretically propose, and experimentally observe a non-trivial non-diffracting wave, the *Bessel beam*, whose electric field spatial part is described by a Bessel function:

$$A(x,y,z) = e^{i\beta z} J_0\left[\alpha(x^2+y^2)\right] \tag{1.13}$$

where $\alpha^2 + \beta^2 = k^2$, and J_0 is the first kind Bessel function of zero order.

Since then, several non-diffracting beams have been realized in 2D , such as Bessel beams, 2D Airy beams, Ring-Airy beams etc. On the other hand, only one non-diffracting solution of the paraxial wave equation exists in 1D [4]. Early in 1978, Berry and Balazs [4] found out theoretically from a quantum mechanical perspective, that there exists a non-trivial wavepacket solution of (1.10) $\psi(z,t)$, whose probability density $|\psi(z,t)|^2$ propagates without distortion. This wavepacket has the initial form $\psi(z, t = 0) = Ai(c \cdot z)$, where with c we denote a product of constants. The function $Ai(z)$, called *Airy function of first kind* or simply *Airy function* [5], is a the one of two linearly independent solutions of *Stokes equation*, $y'' - xy = 0$, and is defined by:

$$Ai(z) = \frac{1}{2\pi i} \int_C e^{\left(t^3/3 + zt\right)} dt \tag{1.14}$$

where C is a path starting at the point at infinity with argument $-\pi/3$ and ending at the point at infinity with argument $\pi/3$.

From the Optics point of view, as shown in 2007 by Siviloglou et al. [6], this optical wavepacket would correspond to a non-trivial solution of (1.9) that propagates without diffraction and carries infinite energy. Apart from their ability to defeat diffraction, these wavepackets have the ability to freely accelerate in the absence of any external potential. We will discuss this later, as well as how these beams are actually realized.

1.4 Angular spectrum method for computational modeling

In general, the angular spectrum method is a technique for modeling the propagation of a wave, whose origin lies in the field of *Fourier Optics* [7]. The basic idea of this method is expressing a field distribution as a superposition of plane waves, and it is mathematically described by a two dimensional Fourier transform [8].

More specifically, let's consider that a wave is incident on the plane $z = 0$ with an initial field distribution $U(x, y; 0)$. Across the plane $z = 0$, the 2D Fourier transform of U is given by [7]:

$$P(k_x, k_y; 0) = \iint U(x, y; 0)e^{-i(k_x x + k_y y)} \, dx \, dy \tag{1.15}$$

Thus, we can express U as the inverse Fourier transform:

$$U(x, y; 0) = \iint P(k_x, k_y; 0)e^{i(k_x x + k_y y)} \, dk_x \, dk_y \tag{1.16}$$

Let's recall that the complex amplitude phasor of a plane wave with wavevector $\vec{k} = k_x \hat{x} + k_y \hat{y} + k_z \hat{z} \equiv k \cos a \cdot \hat{x} + k \cos b \cdot \hat{y} + k \cos c \cdot \hat{z}$ (where a, b, c are the direction angles), for a plane of constant z is given by:

$$u(x, y, z) = e^{i\vec{k} \cdot \vec{r}} = e^{ik(\cos a \cdot x + \cos b \cdot y)} \cdot e^{ik \cos c \cdot z} \tag{1.17}$$

and for $z = 0$ this leads to $u(x, y, 0) = e^{ik(\cos a \cdot x + \cos b \cdot y)} = e^{i(k_x \cdot x + k_y \cdot y)}$. From this expression, it is evident that equation (1.16) is simply a decomposition of U in an infinite sum of plane waves with wavenumbers $(k_x, k_y) = (k \cos a, k \cos b)$ and amplitudes $P(k_x, k_y; 0) \, dk_x \, dk_y$. That's why we refer to (1.15) as the *angular spectrum* of the distribution $U(x, y; 0)$ and we also denote it as $P(k \cdot \cos a, k \cdot \cos b; 0)$.

If we express the field distribution $U(x, y; z)$ for a different plane of constant z using the angular spectrum, by analogy with (1.16) and substitute it in Helmholtz equation (1.4) we conclude that:

$$P(k \cos a, k \cos b; z) = P(k \cdot \cos a, k \cdot \cos b; 0) \cdot e^{ikz\sqrt{1 - \cos^2 a - \cos^2 b}} \tag{1.18}$$
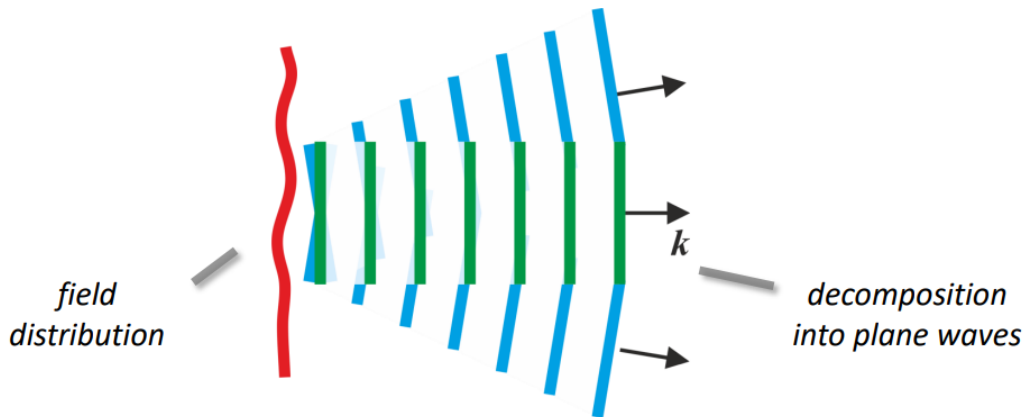

Figure 1.2: Graphical representation of the decomposition of a field distribution at a plane $z = z_0$ into plane waves, as expressed by (1.16). Image source:[9]

So, we find that the field distribution at position z is given by the expression:

$$U(x, y; z) = \iint P(k \cdot cosa, k \cdot cosb; 0) e^{ikz(\sqrt{1-\cos^2 a - \cos^2 b})} e^{ik(\cos a \cdot x + \cos b \cdot y)} \, d(k \cos a) \, d(k \cos b) \Rightarrow$$

$$U(x, y; z) = \iint P(k_x, k_y; 0) \cdot e^{iz(\sqrt{k^2 - k_x^2 - k_y^2})} e^{i(k_x x + k_y y)} \, dk_x \, dk_y \qquad (1.19)$$

This technique gives us the ability to numerically calculate and model the propagation dynamics of a field distribution. The numerical calculations of this thesis have been conducted using the Virtual Lab Wave Propagation Code (*Wp-Maxima*) [10], which uses the angular spectrum method to numerically propagate an 1s scalar optical wave.

Chapter 2

Study of propagation of one-dimensional Airy Beams

2.1 Introduction

In this chapter we will study the propagation characteristics of 1D Airy Beams. As shown by Berry et al. [4] these beams, are non-diffracting solutions of the one dimensional paraxial wave equation:

$$i\frac{\partial u\left(x,z\right)}{\partial z} + \frac{1}{2k}\frac{\partial^2 u\left(x,z\right)}{\partial x^2} = 0 \tag{2.1}$$

where x is the transverse coordinate, z is the propagation distance and k is the wavenumber. The amplitude distribution of Airy beams is described:

$$u\left(x,0\right) = u_0 Ai\left(\frac{x+x_0}{w}\right) \tag{2.2}$$
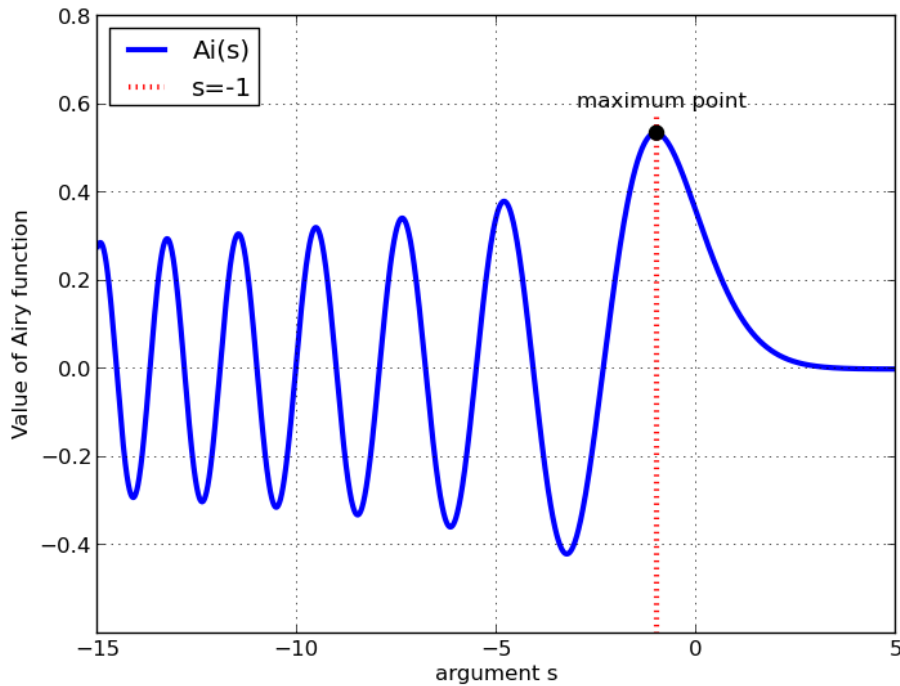

Figure 2.1: Graphical representation of the Airy function $Ai(s)$

where *Ai* is the *Airy* function [8], u_0 is related to the peak amplitude, w is the primary lobe width parameter and x_0 is an offset. The initial field distribution of such a beam is depicted in Fig. 2.1, for the case of $u_0 = 1$ as a function of the dimensionless parameter $s \equiv \frac{x+x_0}{w}$. Note that the Airy function presents a peak value at $s_{max} \simeq -1$. Although these beams are non-diffracting solutions of (2.1), they carry infinite energy so their generation is not realistic. On the other hand, as shown by Siviloglou et al.[11, 12], by applying an appropriate apodization they carry finite energy thus they can be realized. In more detail, using an exponential decay apodization function, the beam amplitude at $z = 0$ becomes:

$$u(x,0) = u_0 Ai\left(\frac{x+x_0}{w}\right) e^{a\frac{x+x_0}{w}} \tag{2.3}$$

where $a > 0$ is an apodization parameter and w and x_0 are respectively the width and peak position parameters of the primary Airy lobe. By solving [12] the 1D wave propagation equation (2.3) we reach to the following analytic solution for the propagation of an apodized 1D Airy beam along z axis:

$$u(x,z) = u_0 Ai\left(\frac{x+x_0}{w} - \frac{z^2}{4k^2w^4} + i\frac{az}{kw^2}\right) e^{a\left(\frac{x+x_0}{w} - \frac{az^2}{2k^2w^4}\right)} e^{i\left(\frac{a^2z}{2kw^2} + \frac{x_0+x}{2kw^3}z - \frac{z^3}{12k^3w^6}\right)} \tag{2.4}$$

This leads to an intensity $I(x,z)$ given by:

$$I(x,z) = I_0 \left| Ai\left(\frac{x+x_0}{w} - \frac{z^2}{4k^2w^4} + ia\frac{z}{kw^2}\right) \right|^2 e^{2a\frac{x+x_0}{w} - a\frac{z^2}{k^2w^4}} \tag{2.5}$$

where for small apodization parameters $a \ll 1$ we can drop the imaginary term in the argument of Airy Function, and so (2.5) is simplified to:

$$I(x,z) = I_0 \left| Ai\left(\frac{x+x_0}{w} - \frac{z^2}{4k^2w^4}\right) \right|^2 e^{2a\frac{x+x_0}{w} - a\frac{z^2}{k^2w^4}} \tag{2.6}$$

2.2 Trajectory of the Airy primary lobe

Airy beams propagate in an unconventional way [4, 11, 12]. They resist to diffraction and follow a curved trajectory as they propagate. The trajectory of the primary lobe of an Airy beam can be estimated by solving Eq.(2.6) for $Ai(s_{max})$, where $s_{max} \simeq -1$:

$$x_{max}(z) = -(x_0 + w) + \frac{1}{4k^2w^3} \cdot z^2 \tag{2.7}$$

From this equation it is apparent that the primary beak of an 1D Airy beam follows a parabolic trajectory as the beam propagates, a characteristic that led to the characterization of these beams as "accelerating". [11]

Using numerical simulations [10] we can confirm the validity of the analytically derived Eq. (2.7). In our numerical simulations we alter each time a single parameter (e.g. w) while keeping the other parameters constant (e.g. k and z) and we compare the $x_{max}(z)$ values to the theoretical predictions of Eq. (2.7). At all the numerical experiments, we chose to set the apodization parameter $a = 0.05$ and the peak position parameter to $x_0 = 0$.

A typical simulation result of the intensity $I(x,z)$ distribution of a propagating Airy beam is shown in Fig. 2.2. As we clearly see, the primary peak of the beam follows a curved trajectory that, as we are going to confirm in the analysis that follows, is parabolic.
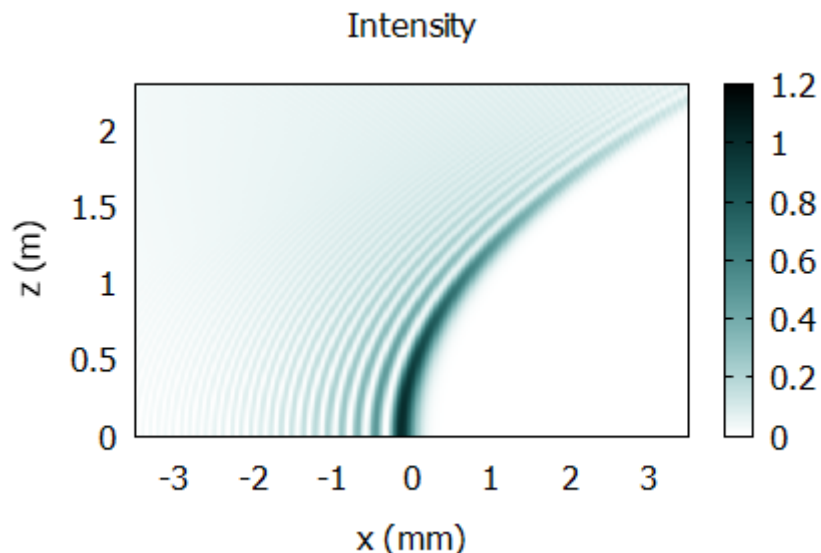
Figure 2.2: *Propagation of a typical Airy beam in 1D+1 regime.* $(w = 200 \ \mu m, x_0 = 0, \ \lambda = 800 \ nm, a = 0.05)$

In order to confirm the validity of the theoretical prediction of Eq. (2.7) we performed numerical simulations [10] of the propagation of Airy beams. In our simulations we firstly kept $w = const = 100 \ \mu m$ while varied the wavelength for $\lambda = 400$ nm $\rightarrow 800$ nm with a $100 nm$ step. In each numerical experiment we retrieved the peak position x_{max} at fixed propagation distance $z = 500.2$ mm. In the following Table 2.1 we display our numerical results, compared to the corresponding theoretical predictions from equation (2.7).

Please note that the discretization error of our numerical measurements was, each time, orders of magnitude smaller than the measuring physical quantity.

At the following Figure 2.3 we have plotted in the same diagram both the theoretical curve as predicted by equation (2.6) and the numerical results of the peak position x_{max} as a function of wavelength λ (for constant w and z).

Table 2.1

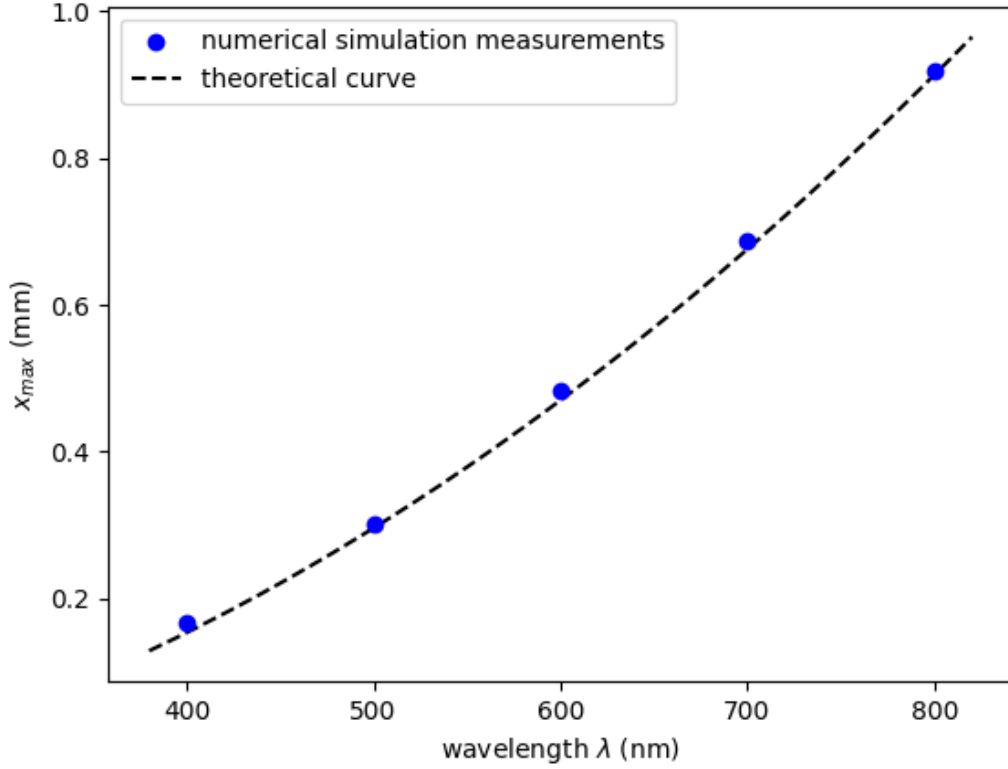| wavelength	theoretical prediction	numerical simulation	difference
λ(nm)	x_{max}(mm)	x_{max}(mm)	(%)
400	0.1535	0.1660	8.14
500	0.2961	0.3027	2.23
600	0.4704	0.4833	2.74
700	0.6764	0.6877	1.67
800	0.9140	0.9180	0.44

Figure 2.3: *Theoretical curve and numerical results of the peak position x_{max} as a function of wavelength λ*

We clearly see that our numerical results are in very good agreement with the analytical predictions.

Then, we kept the wavelength, and thus k, constant to $\lambda = 800$ nm, while varying the value of the width parameter w. We ran numerical simulations altering the value of w, from $w = 80\mu$m $\rightarrow$ w $= 160\mu$m with an 20μm step. Again, in each numerical experiment we retrieved the peak position x_{max} at fixed propagation distance $z = 500.2$ mm. Our numerical results, compared to the corresponding theoretical predictions from equation (2.7) are shown in in Table 2.2.

Table 2.2

wavelength	theoretical prediction	numerical simulation	difference
λ(nm)	x_{max}(mm)	x_{max}(mm)	(%)
80	1.901	1.904	0.15
100	0.914	0.918	0.48
120	0.4668	0.4785	2.5
140	0.2295	0.2442	6.4
160	0.0876	0.1074	22.6

At the following Figure 2.4 we have plotted in the same diagram both the theoretical curve as predicted by equation (2.6) and the numerical results of the peak position x_{max} as a function of the width parameter w (for constant k and z).
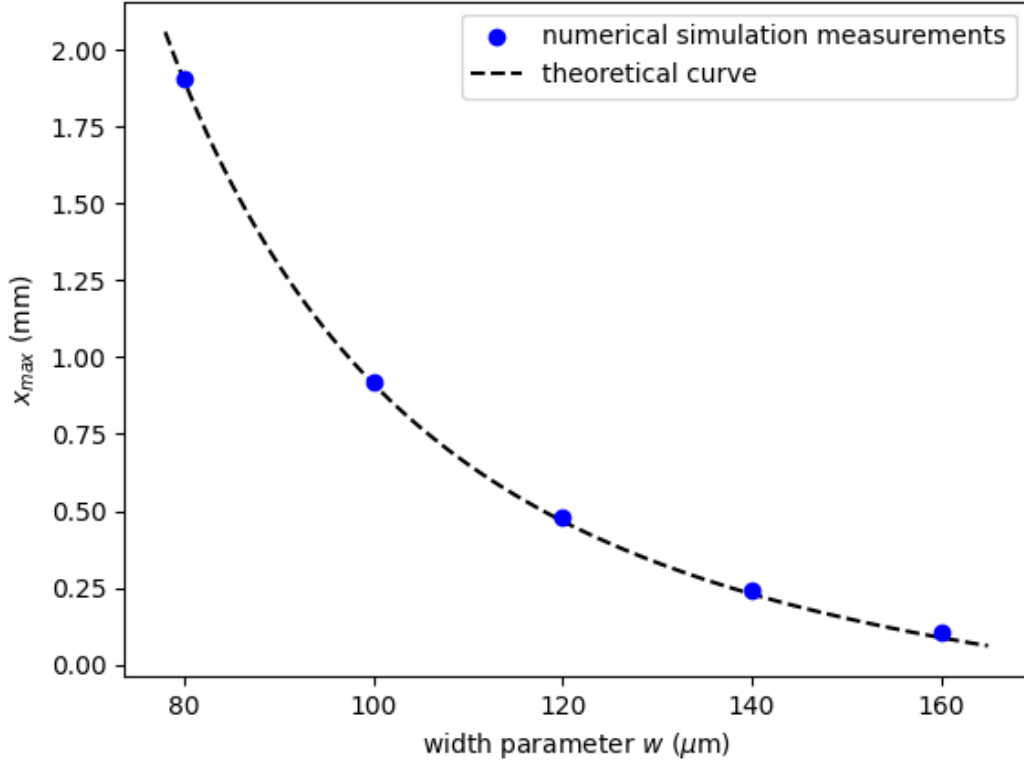
13

Figure 2.4: *Theoretical curve and numerical results of the peak position x_{max} as a function of width parameter w*

Again, we conclude that our numerical results are in good agreement with the analytical expression of equation (2.7).

Lastly, we kept the wavelength and the width parameter constant, $\lambda = 800$ nm, w $= 100$ μm and we tracked the peak position x_{max} for various propagation distances. In Table 2.3 we display our numerical results, compared to the corresponding theoretical predictions from equation (2.6).

Table 2.3

propagation distance	theoretical prediction	numerical simulation	difference
z(m)	x_{max}(mm)	x_{max}(mm)	(%)
0.1005	-0.0590	-0.0488	17.3
0.2003	0.0626	0.0781	24.7
0.3000	0.2647	0.2734	3.3
0.4005	0.5501	0.5567	1.2
0.5002	0.9140	0.9180	0.4

Furthermore, in Fig. 2.5 we plot in the same diagram both the theoretical curve as predicted by equation (2.7) and the numerical results of the peak position x_{max} as a function of propagation distance z.
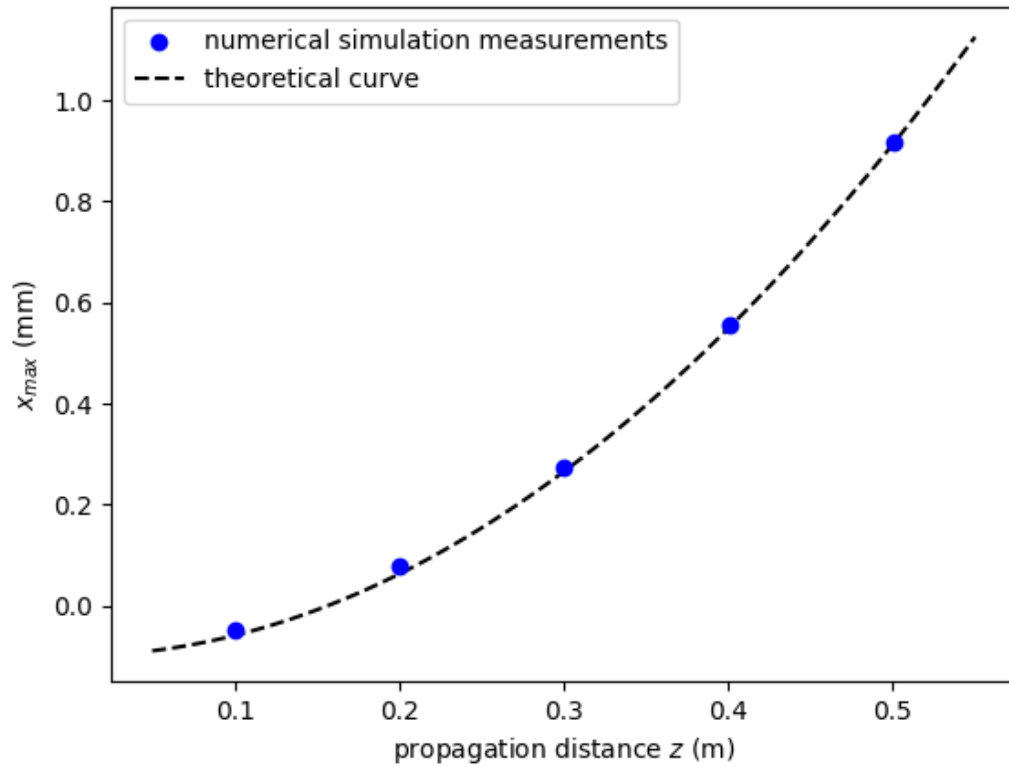
Figure 2.5: *Theoretical curve and numerical results of the peak position x_{max} as a function of propagation distance z*

As we can clearly see, our numerical results are in excellent agreement with the analytical prediction of Eq. (2.6). Likewise, we have straightforward demonstration of the parabolic trajectory of the Airy beam primary lobe.

2.3 Rayleigh range of one-dimensional Airy beams

As already mentioned in Section 1.4, the one-dimensional Airy beam has a unique characteristic; it is the only non-trivial non-diffracting solution of the paraxial wave equation in 1D[4, 13]. Of course, for small but non-zero values of the apodization factor a, which is the only realistic case, the one-dimensional Airy beam tends to diffract slightly and can only be described as *quasi non-diffracting* [14]. That means that, for $a << 1$, apodized Airy beams compared to Gaussian beams diffract in a much slower rate thus can be considered as "diffraction free" for all the practical purposes. We will now study this property using numerical simulations [10].

At first, we simulate the propagation of a Gaussian beam with wavelength $\lambda = 800nm$ and $FWHM = 228\mu m$. Then, we simulate the propagation of an 1D Airy beam of the same wavelength and main lobe's $FWHM$, with apodization factor $a = 0.05$. In Fig. 2.6 we show the $I(x, z)$ intensity distributions and the peak intensity $I_{max}(z)$ for case of 1D Airy and Gaussian beams.
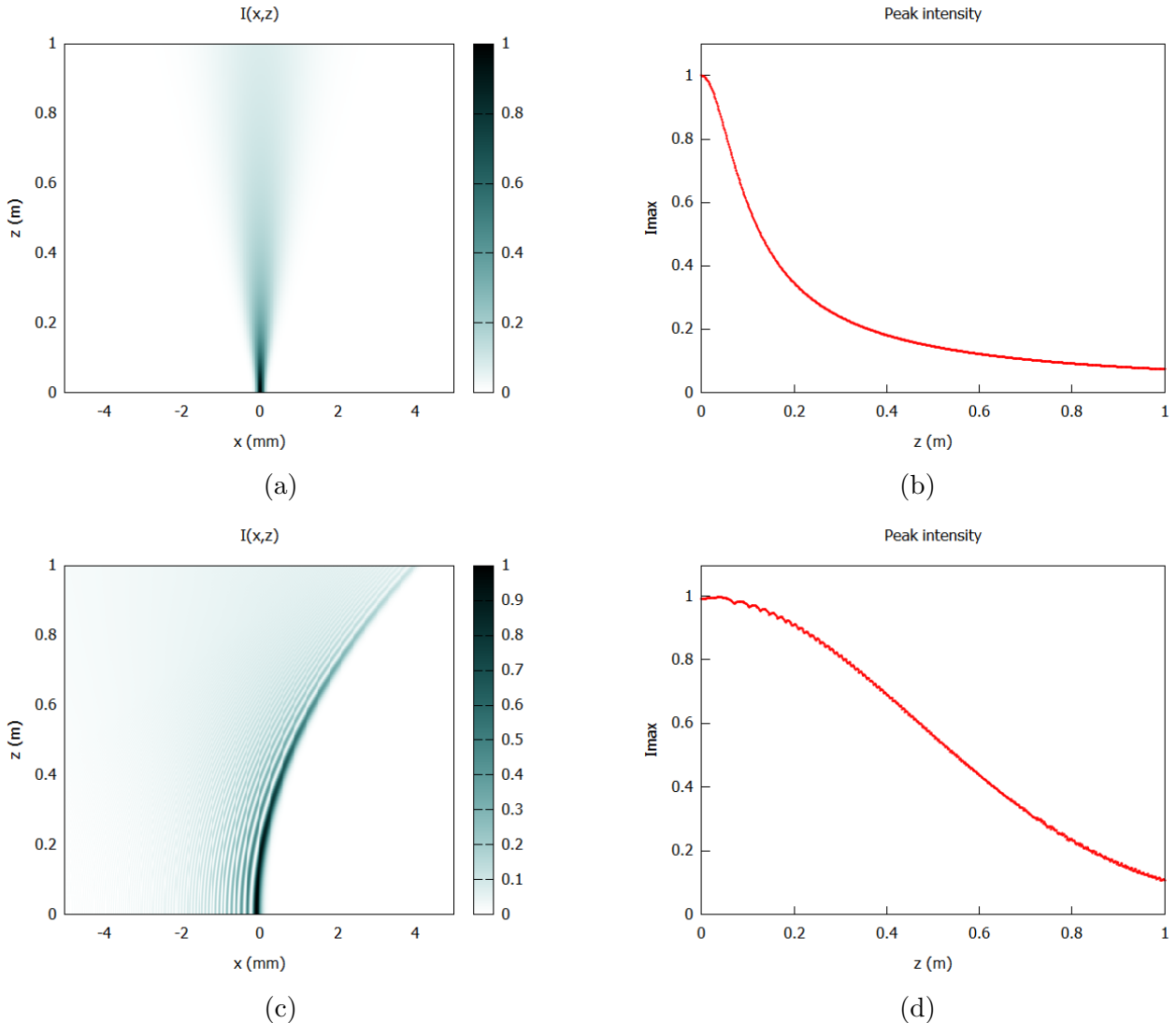

(a)

(b)

(c)

(d)

Figure 2.6: Comparison $I(x, z)$, $I_max(z)$ for an Gaussian and Airy beam with $\lambda = 800nm$, $FWHM = 228\mu m$ and $a = 0.05$

From the above numerical experiments, we measured the propagation distances from $z = 0$ at which the intensity of the primary peak has dropped to the half of its initial value, often

referred to as *Rayleigh range* z_r [1] for the two-dimensional Gaussian Beams. We measured the Rayleigh range of the Gaussian beam z_r^G equal to $z_r^G = 0.1267m$, and the Rayleigh range of the Airy beam z_r^{Ai} equal to $z_r^{Ai} = 0.55m$. So, we numerically confirmed that a truncated one-dimensional Airy Beam can, indeed, be described as non-diffracting, in comparison with the Gaussian Beam.

We would now like to find a theoretical relation for the *Rayleigh range* z_r^{Ai} of an Airy beam at 1D+1 regime, in analogy to a Gaussian Beam's $z_r^G \equiv z_R$ that we represented in Eq. (4.28), That is, by definition (here we use the property of 2D, instead of 1D, beams), the *Rayleigh range* is defined as the distance from $z = 0$ that the beam propagates until it's peak intensity drops to half of its initial value $I(x_{max}, z_r^{Ai}) = \frac{I(x_{max},0)}{2}$.

At first, using Eq. (2.7) we replace for $x_{max}(z)$ to Eq. (2.6) (setting for simplicity $x_0 = 0$) that describes the intensity beam intensity $I(x, z)$ to estimate peak intensity distribution $I_{peak}(z) \equiv I(x_{max}, z)$:

$$I(x_{max}, z) = I_0 \left| Ai(-1) \right|^2 e^{\frac{2a}{w}\left(-w+\frac{z^2}{4k^2w^3}\right)-a\frac{z^2}{k^2w^4}} = I_0 \left| Ai(-1) \right|^2 e^{-2a} e^{-\frac{az^2}{2k^2w^4}} \tag{2.8}$$

Demanding from $I(x_{max}, z_r^{Ai})$ to satisfy the condition $I(x_{max}, z_r^{Ai}) = \frac{I(x_{max},0)}{2}$ we finally get:

$$z_r^{Ai} = \frac{kw^2}{\sqrt{a}}\sqrt{2\ln 2} \tag{2.9}$$

Having derived (2.9) theoretically, we wish to check its validity, conducting numerical experiments [10].

At first, we kept the apodization factor a and the wavelength λ fixed to the values $a = 0.05$ and $\lambda = 800nm$, respectively, and changed the width parameter w from $w = 60\mu m$ to $w = 140\mu m$ with a $20\mu m$ step. For each value of the width parameter w, we numerically found the propagation distance $z = z_r^{Ai}$, at which the intensity of the beam has dropped to $1/2$ of its initial value. We display our numerical results compared to the theoretical predictions of equation (2.9) at the following Table 2.4.

Table 2.4

width parameter	theoretical prediction	numerical simulation	difference
$w(\mu m)$	$z_r^{Ai}(\mu m)$	$z_r^{Ai}(\mu m)$	(%)
60	0.1489	0.1568	5.3
80	0.2647	0.2782	5.1
100	0.4135	0.4357	5.4
120	0.5955	0.6262	5.2
140	0.8106	0.8512	5.0

At the following Figure 2.7 we have plotted in the same diagram both the theoretical curve as predicted by equation (2.9) and the numerical results of the Rayleigh range z_r^{Ai} as a function of the width parameter w.
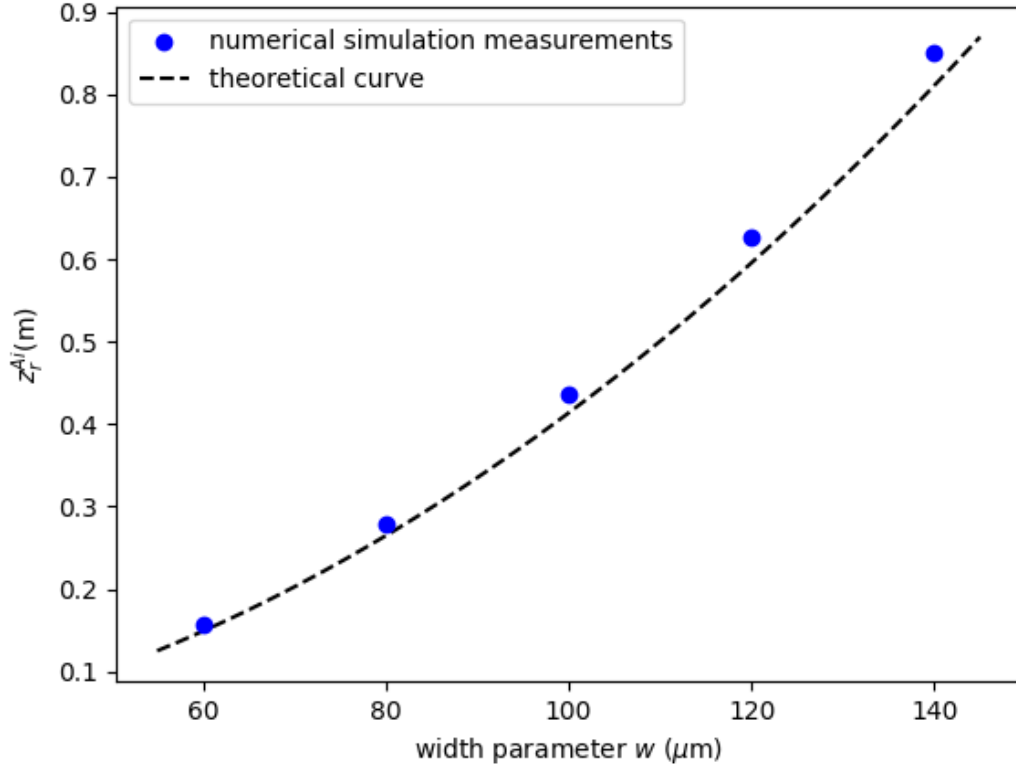
Figure 2.7: *Theoretical curve and numerical results the Rayleigh range z_r^{Ai} as a function of the width parameter w.*

Although our numerical results are in fair agreement with the theoretical prediction, we clearly observe a systematic discrepancy between them. In fact, the discrepancy seems to increase as the width parameter w increases.

Then, we kept a and w constant to $a = 0.05$, $w = 100$ μm and changed the wavelength λ, thus and the wavenumber k. In our numerical simulations, the wavelength λ, ranged from $\lambda = 600nm$ to $\lambda = 1000nm$ with a $100nm$ step. In each simulation we identified the propagation distance $z = z_r^{Ai}$, at which the intensity of the beam has dropped to $1/2$ of its initial value. In Table 2.5 we display our numerical results, compared to the corresponding theoretical predictions from Eq. (2.9).

Table 2.5

wavelength	theoretical prediction	numerical calculation	difference
λ(nm)	z_r^{Ai}(μm)	z_r^{Ai}(μm)	(%)
600	0.5514	0.5810	5.4
700	0.4726	0.4981	5.4
800	0.4136	0.4357	5.3
900	0.3676	0.3875	5.4
1000	0.3308	0.3488	5.4

In Fig. 2.8 we have plotted in the same diagram both the theoretical curve as predicted by equation (2.9) and the numerical results of the Rayleigh range z_r^{Ai} as a function of the wave-

length λ.

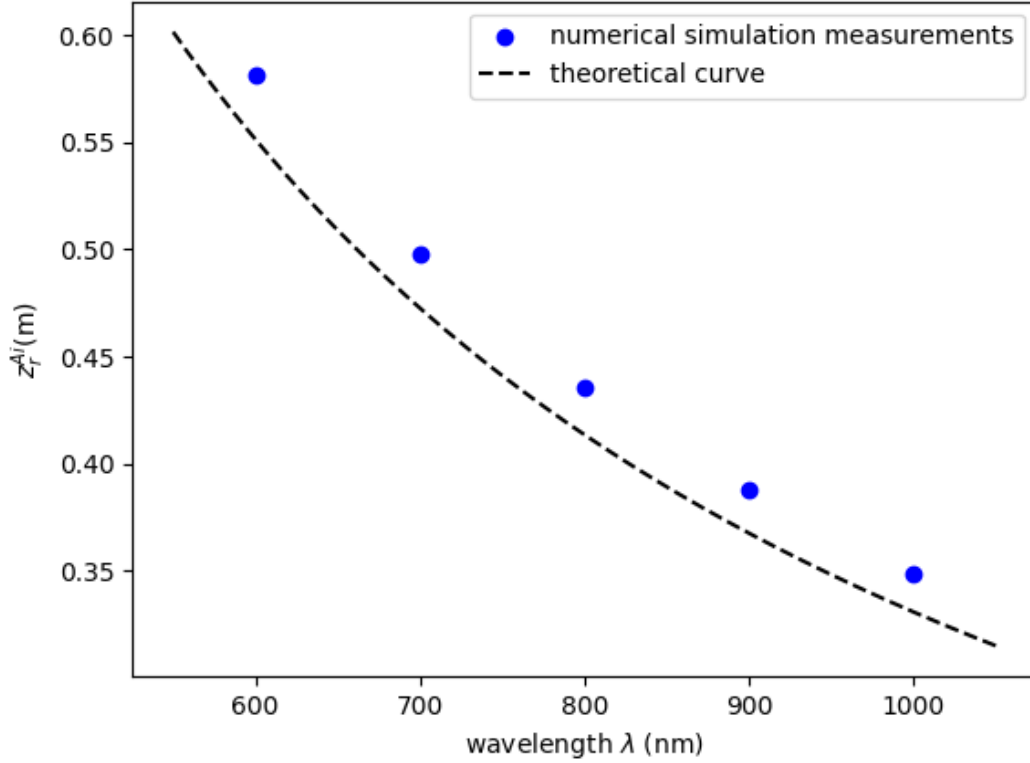Figure 2.8: *Theoretical curve and numerical results the Rayleigh range z_r^{Ai} as a function of the wavelength λ.*

Again, our numerical results are in good agreement with the theoretical curve. But, it is clearly visible, again, that a systematic divergence between the numerical results and the curve exists. Moreover, it seems to get increased while the wavelength λ decreases.

Lastly, we kept λ and w constant to the values $\lambda = 800nm$, $w = 100\mu m$ and changed the value of the apodization factor a. We ran numerical simulations for five different values of a. For each different a, we numerically measured the propagation distance $z = z_r^{Ai}$, at which the intensity of the beam has dropped to $1/2$ of its initial value. In the following Table 2.6 we display our numerical results, compared to the corresponding theoretical predictions from equation (2.9).

Table 2.6

apodization factor	theoretical prediction	numerical calculation	difference
a	$z_r^{Ai}(\mu m)$	$z_r^{Ai}(\mu m)$	$(\%)$
0.03	0.5339	0.5528	3.5
0.05	0.4135	0.4357	5.4
0.1	0.2924	0.3245	11.0
0.15	0.2388	0.2791	16.9
0.2	0.2068	0.2550	23.3

At the following Figure 2.9 we have plotted in the same diagram both the theoretical curve as predicted by equation (2.9) and the numerical results of the Rayleigh range z_r^{Ai} as a function of the apodization parameter a.
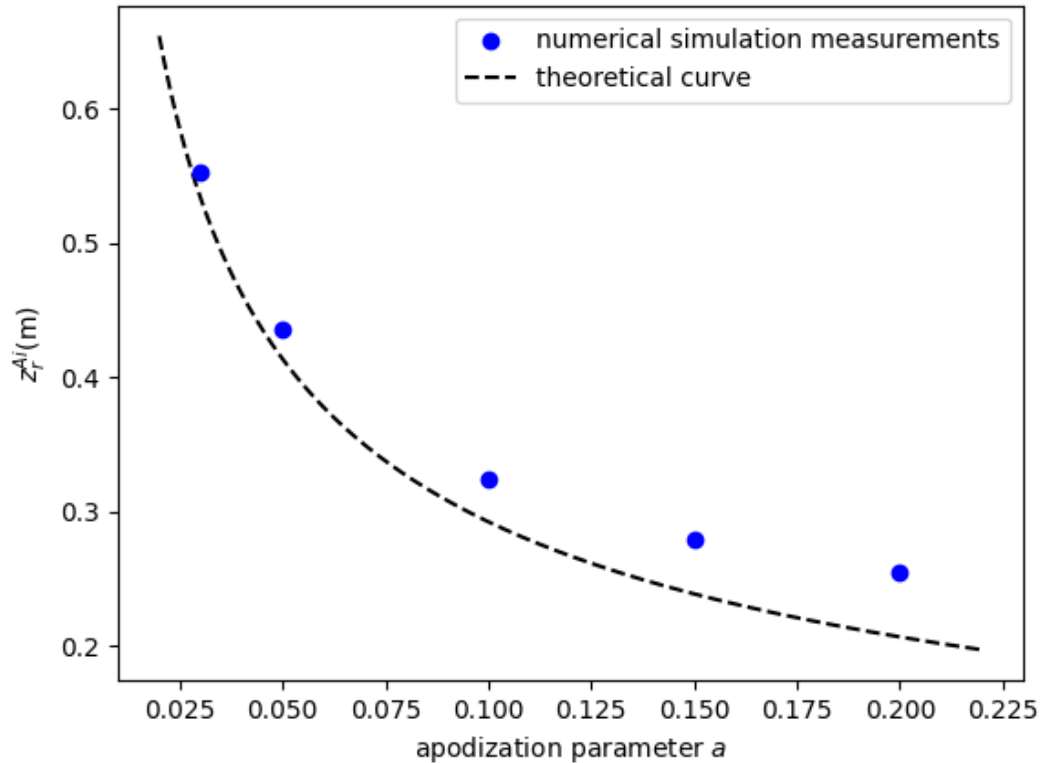

Figure 2.9: *Theoretical curve and numerical results the Rayleigh range z_r^{Ai} as a function of apodization parameter a.*

As we can observe, the numerical results diverge, at an increasing rate, from the theoretical prediction as the apodization parameter a is increased.

The origin of this systematic error, lies on the assumptions under which the Eq. (2.9) is valid. Already from Eq. (2.6), we assumed that the imaginary term of the Airy function's argument has a negligible effect on the Airy function values thus it can be neglected. This assumption is valid only for very small values of the apodization parameter, and it leads to an increasing underestimation of the Rayleigh range z_r^{Ai}, already observed in Figs 2.6-2.8.

In order to better understand this effect, let us firstly introduce the more convenient dimen-

sionless notation $s \equiv x/w$, $\xi \equiv z/kw^2$. Using this we can describe the the Airy function term of Eq. (2.5) as

$$f_a(s_{max}) \equiv Ai(s_{max} + \frac{\xi_r^2}{4} + ia\xi_r) \tag{2.10}$$

where $\xi_r = z_r^{Ai}/kw^2$ is given by $\xi_r = \sqrt{\frac{2\ln 2}{a}}$. This is the *exact* form of the Airy function that we used in Eq. (2.6), assuming that $a \to 0$.

For the limiting case of $a = 0$, we obtain

$$f_0(s_{max}) = Ai(s_{max} + \frac{\xi_r^2}{4}) \tag{2.11}$$

which is the Airy function that we used in equation (2.6).

Let us now define the *difference* function:

$$D_a(s_{max}) = |f_a(s_{max})|^2 - |f_0(s_{max})|^2 \tag{2.12}$$

that gives as the difference between the accurate value of the Airy beam's intensity and the approximate value of Airy beam's intensity $I(x, z_r^{Ai})$ that we used in Eq. (2.8) (assuming $a \to 0$), as a function of the dimensionless peak's transverse coordinate s_{max}.

In Fig. 2.10, we show the functions $|f_0(s_{max})|^2$, $|f_{0.05}(s_{max})|^2$, $|f_{0.1}(s_{max})|^2$ and the difference function $D_{0.05}(s_{max})$.
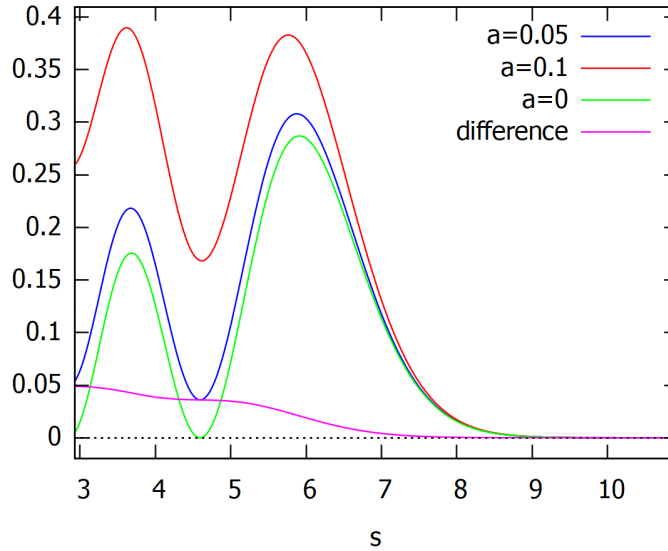

Figure 2.10

From Fig. 2.10 we clearly observe that as a is increased the peak the systematic divergences that we observed at Figures 2.7, 2.8 and 2.9. First of all, the beam's intensity at the distance that we regarded as Rayleigh range z_r^{Ai}, is always **greater** than the intensity that it would have if a was equal to 0. Thus, the beam will have to propagate for a distance further than z_r^{Ai} in order to obtain an intensity that truly is equal to half the initial intensity. *The reason why all our numerical measurements for the Rayleigh range were greater than the theoretical prediction has now been revealed.*.

Furthermore, Figure 2.10 shows that this divergence will become greater, as the apodization factor a is increased. That explains the behavior of the divergence at Figure 2.9.

Lastly, is is clear from Figure 2.10 that the difference vanishes if the Rayleigh range (as predicted by (2.9)) corresponds to large values of the primary peak transverse coordinate ($s_{max} \geqslant 7$). On the other hand, for values of $s_{max} < 7$, the difference increases when s_{max} becomes lower. That explains the behavior of the divergences at Figures 2.8 and 2.9; from Figures 2.3 and 2.4 we know that while k or w increases, the primary peak's transverse coordinate s_{max} decreases, and that's the reason why the corresponding divergences increase.

2.4   Reduction of one-dimensional Airy beam to Gaussian-like beam

We now want to discuss how Airy Beams at 1D+1 regime behave when the apodization factor a takes large values. It will be revealed easily that, in fact, Airy Beams are reduced to our well-known Gaussian Beams. We recall from equation (2.3) that the initial condition for $z = 0$ is a product of an Airy function and an exponential decay function, namely (for $x_0 = 0$):

$$u\left(x,0\right) = u_0 Ai\left(\frac{x}{w}\right) e^{a\frac{x}{w}} \tag{2.13}$$

In order to realize the qualitative characteristics of this initial field distribution, we plot it as a function of the dimensionless transverse coordinate parameter $\frac{x}{w}$ for various values of the apodization factor a. We represent these beam profiles in the following Figure 2.11.
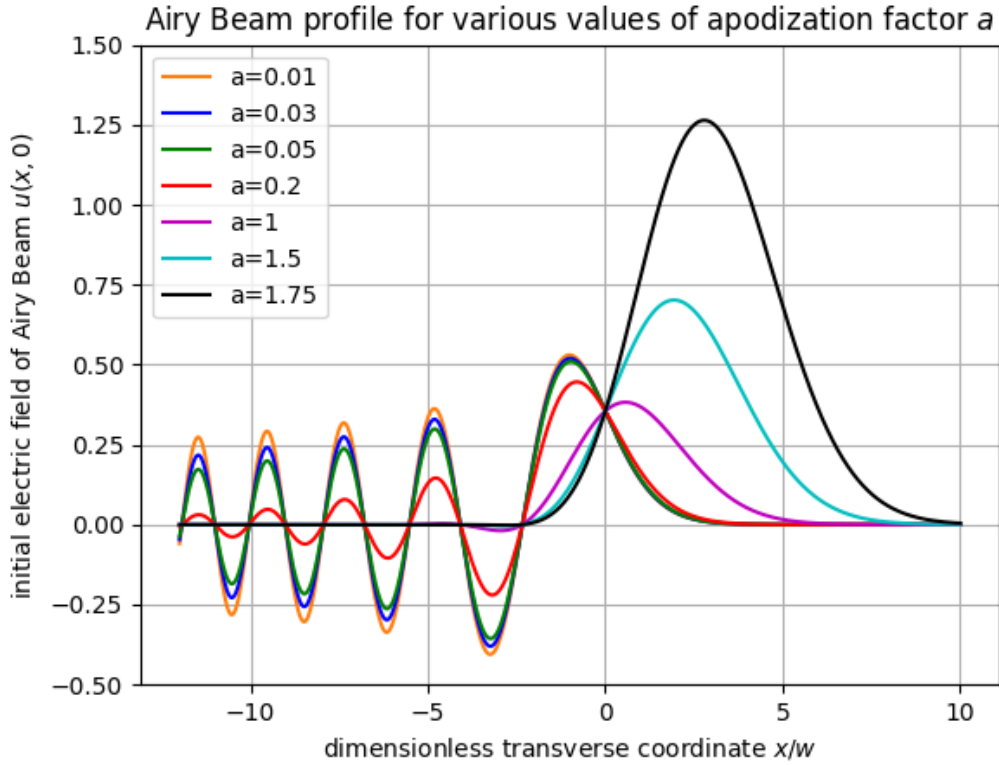

Figure 2.11: *Airy Beam field profile for various values of the apodization factor α*

Looking to the previous diagram, we find out that while a is increasing, the main lobe shifts to the positive direction of x-axis and gets greater values, while the secondary lobes

shrink and tend to disappear. For $a \geqslant 1$ the beam's profile consists only of a main peak that has a Gaussian-like shape. So, we conclude that the propagation of an Airy beam with

(a) $a = 0.01$

(b) $a = 0.03$

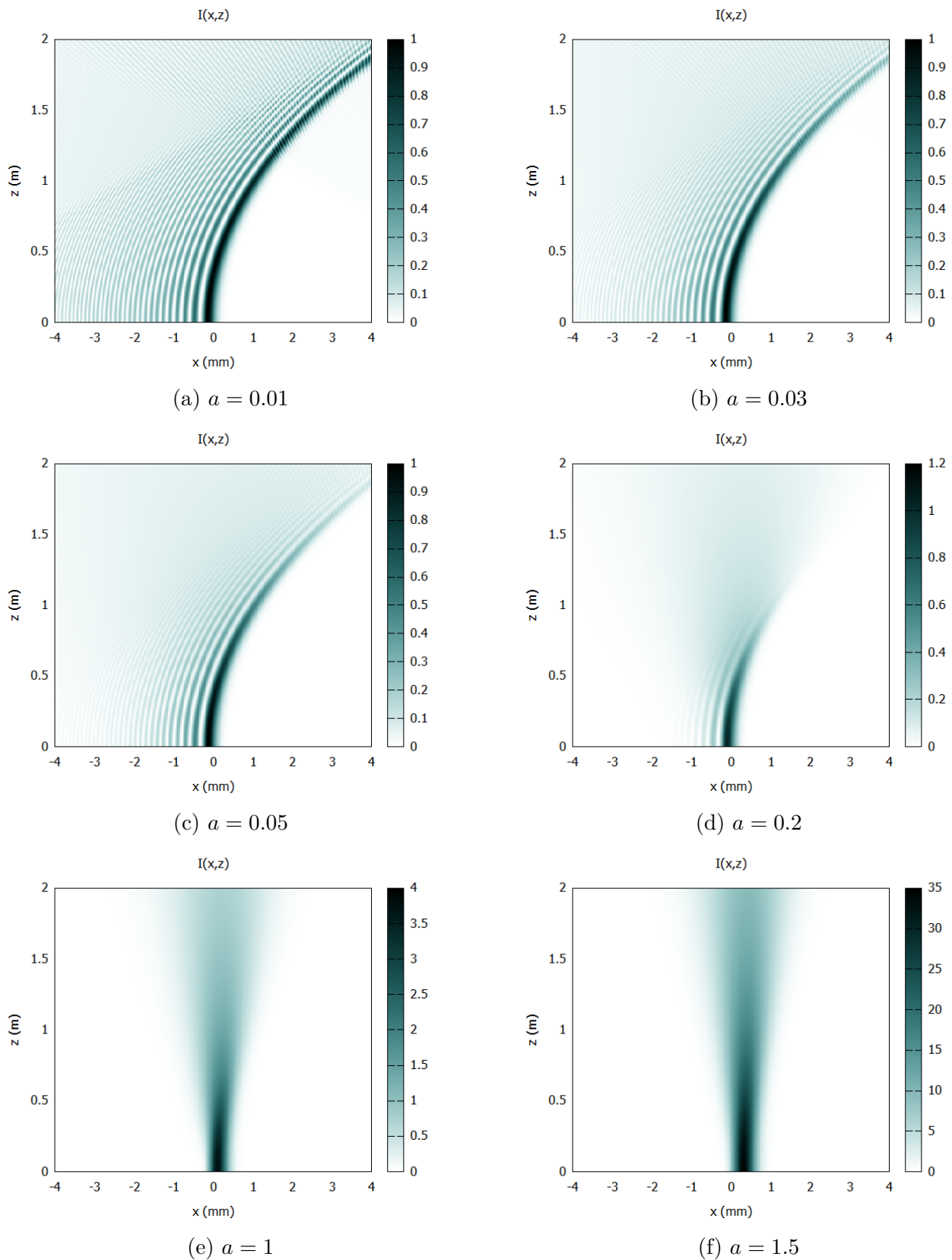(c) $a = 0.05$

(d) $a = 0.2$

(e) $a = 1$

(f) $a = 1.5$

Figure 2.12: Propagation image of an Airy Beam with $\lambda = 800nm$, $w = 150\mu m$ for various apodization parameters

a large apodization factor a at 1D+1 regime will be similar to that of a Gaussian Beam. We still have to confirm this numerically, and we will do it conducting numerical simulations with $Wp - Maxima$ as previously.

Running the simulation code for six different values of a, correspondingly with Figure 2.12, we see the following image for the propagation over $z - axis$, together with the intensity of the beam at each point in the attached colourmap.

It can be deduced from these propagation images that for $a \geqslant 1$ the Airy Beam has indeed been reduced to a Gaussian-like beam. Already for $a = 0.2$, as we see in Figure 2.12d, the beam has lost its interesting property to have a parabolic moving primary peak.

2.5 Self-healing property of one-dimensional Airy beams

At the last part of this chapter, we will discuss the property of Airy Beams to self-reconstruct during propagation after being intercepted by obstacles [15],[16], [17]. This characteristic is very important, when such beams propagate in inhomogeneous media and have the ability to reform after several perturbations [18]. This property has a very simple and beautiful physical origin, as it is a result of ***Babinet' s principle*** for non-diffracting beams [19].

Generally, as we discussed in Chapter 1, a beam, in free space, is described as *non-diffracting* when its intensity profile $I \sim |u_I|^2$ remains constant during propagation. Let's suppose an initially non-diffracting beam at 1D+1 regime, whose complex amplitude u_I is disturbed by an obstacle of width D placed at $z = z_0$. As a consequence of *Babinet' s Principle*, the amplitude of the disturbed field, in the half plane $z > z_0$ is given by:

$$u_D = u_I - u_C \tag{2.14}$$

where with u_C we denote the complex amplitude of the field diffracted by an hypothetical aperture of width D, complementary to the obstacle.

Since the complex amplitude u_C decreases as $1/z$ under propagation, the contribution of this term in equation (2.14) for propagation distance $\Delta z > \frac{\pi D^2}{\lambda} \equiv z_H$ can be neglected. Thus, due to the non-diffracting nature of the beam, the total amplitude u_D after propagation distance $z - z_0 > z_H$ will be practically equal to u_I. This property of all non-diffracting beams is referred in the literature as *self-healing* [20].

Applying these simple arguments for the case of one-dimensional Airy beams, which can be assumed as non-diffracting for small values of apodization factor a, we can predict their self - reconstructing behaviour. We will try to observe the self - healing property of one-dimensional Airy Beams conducting numerical experiments with $Wp - Maxima$ as usual.

At first, we wish to visually verify the validity of expression (2.14), which explains this self - reconstructing behaviour. For this purpose we conducted two numerical simulations for an 1-D Airy beam of $\lambda = 800$ nm and apodization factor $a = 0.02$. At the first, we chose the FWHM of the primary lobe equal to $w_g = 456$ μm and placed a block of width $D = 2w_g = 912$ μm at propagation distance $z_0 = 0.4$ m and transverse position $x = -0.4$ mm. At the second, we chose the FWHM of the primary lobe equal to $w_g = 228 \mu m$ and placed a block of width $D = w_g/2 = 114$ μm at propagation distance $z = 0.05$ m and transverse position $x = -0.1$ mm. For both configurations, we then repeated the simulation, replacing the block with the complementary aperture of the same width D. We represent the simulation outputs for the beams' propagation over z-axis, together with attached colour-maps that correspond to the intensity, at the following Figure 2.13. We also represent the propagation images of the corresponding beams without the presence of a block or an aperture.

(a) $w_g = 456\mu m$, block width $D = 912\mu m$

(b) $w_g = 456\mu m$, aperture width $D = 912\mu m$

(c) $w_g = 456\mu m$, free propagation

(d) $w_g = 228\mu m$, block width $D = 114\mu m$

(e) $w_g = 228\mu m$, aperture width $D = 114\mu m$

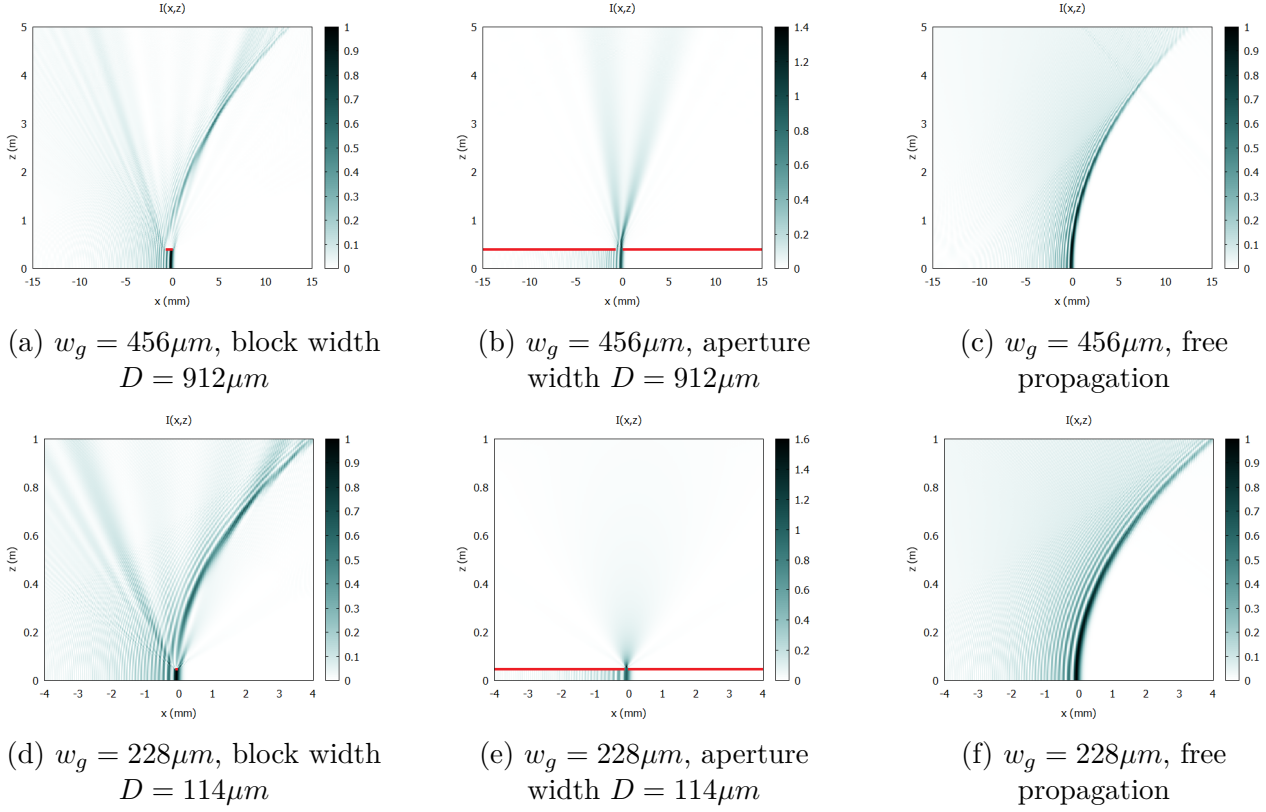(f) $w_g = 228\mu m$, free propagation

Figure 2.13: Propagation of Airy beams in free space and under the action of various obstacles. (a),(d): the beam is partially blocked by a finite obstacle. (b), (e) an aperture (complementary to the obstacle) allows only a portion of the beam to pass through. (c),(f) free propagation

It is clear from this Figure that the image of propagation of the beam with the presence of a block(Figures 2.13a and 2.13d) is complementary to the image of propagation of the beam with the presence of a corresponding aperture(Figures 4.1b and 2.12e); the combinations of these two pairs gives normal propagation images of free 1-D Airy beams 2.12c and 2.12f. So, after visualizing the application of Babinet' s principle to the case of one-dimensional Airy Beams, we wish to turn our attention to their self-healing property.

Firstly, we ran numerical simulations having chosen apodization factor $a = 0.02$, wavelength $\lambda = 800$ nm, FWHM of the primary lobe $w_g = 228$ μm and having placed a block at propagation distance $z_0 = 0.05$ m and transverse coordinate $x = -0.1$ mm. At each simulation we changed the width of the block D. At the following Table 7 we calculate the expected typical distance of self-reconstruction, z_H for the various block widths. Furthermore, at the next Figure 2.14 we display the corresponding images of propagation.

Table 2.7

Block width $D(\mu m)$	Expected Self-Healing distance $z_H(m)$
114	0.05
228	0.20
456	0.82

26

(a) block width $D = 114\mu m$
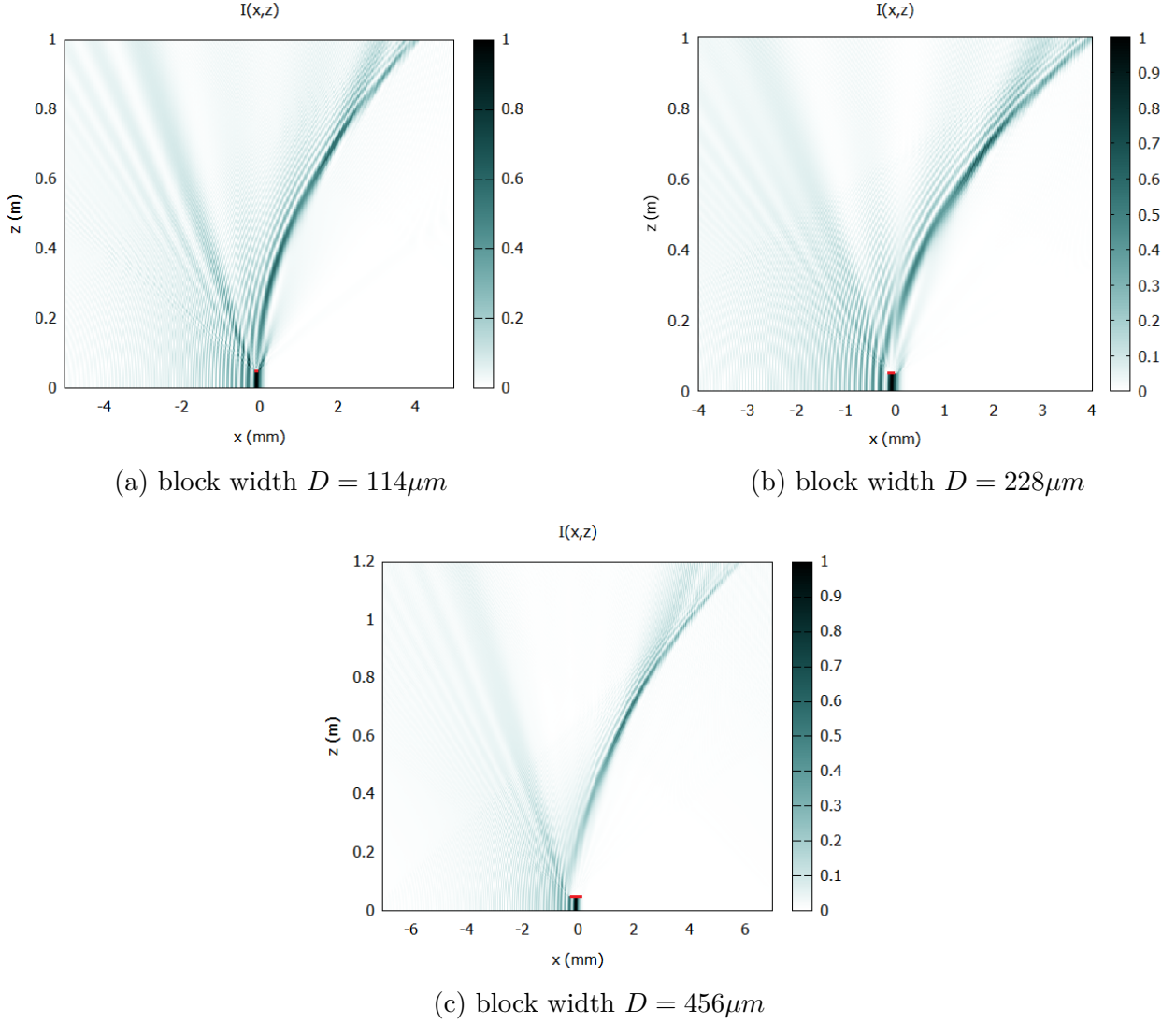

(b) block width $D = 228\mu m$

(c) block width $D = 456\mu m$

Figure 2.14: Self-reconstruction of one-dimensional Airy Beam with $\lambda = 800nm$, $w_g = 228\mu m$ that is intercepted by an obstacle of various widths D, placed at $z = 0.05m$, $x = -0.1mm$

Then, we ran numerical simulations having chosen apodization factor $a = 0.02$, wavelength $\lambda = 800$ nm, FWHM of the primary lobe $w_g = 456$ μm and having placed a block at propagation distance $z = 0.2$ m and transverse coordinate $x_0 = -0.2$ mm. At each simulation we changed the width of the block D. At the following Table 8 we calculate the expected typical distance of self-reconstruction, z_H for the various block widths. Furthermore, at the next Figure 2.15 we display the corresponding images of propagation.

Table 2.8

Block width $D(\mu m)$	Self-Healing expected distance $z_H(m)$
228	0.20
456	0.82
912	3.27

27

(a) block width $D = 228\mu m$

(b) block width $D = 456\mu m$

(c) block width $D = 912\mu m$
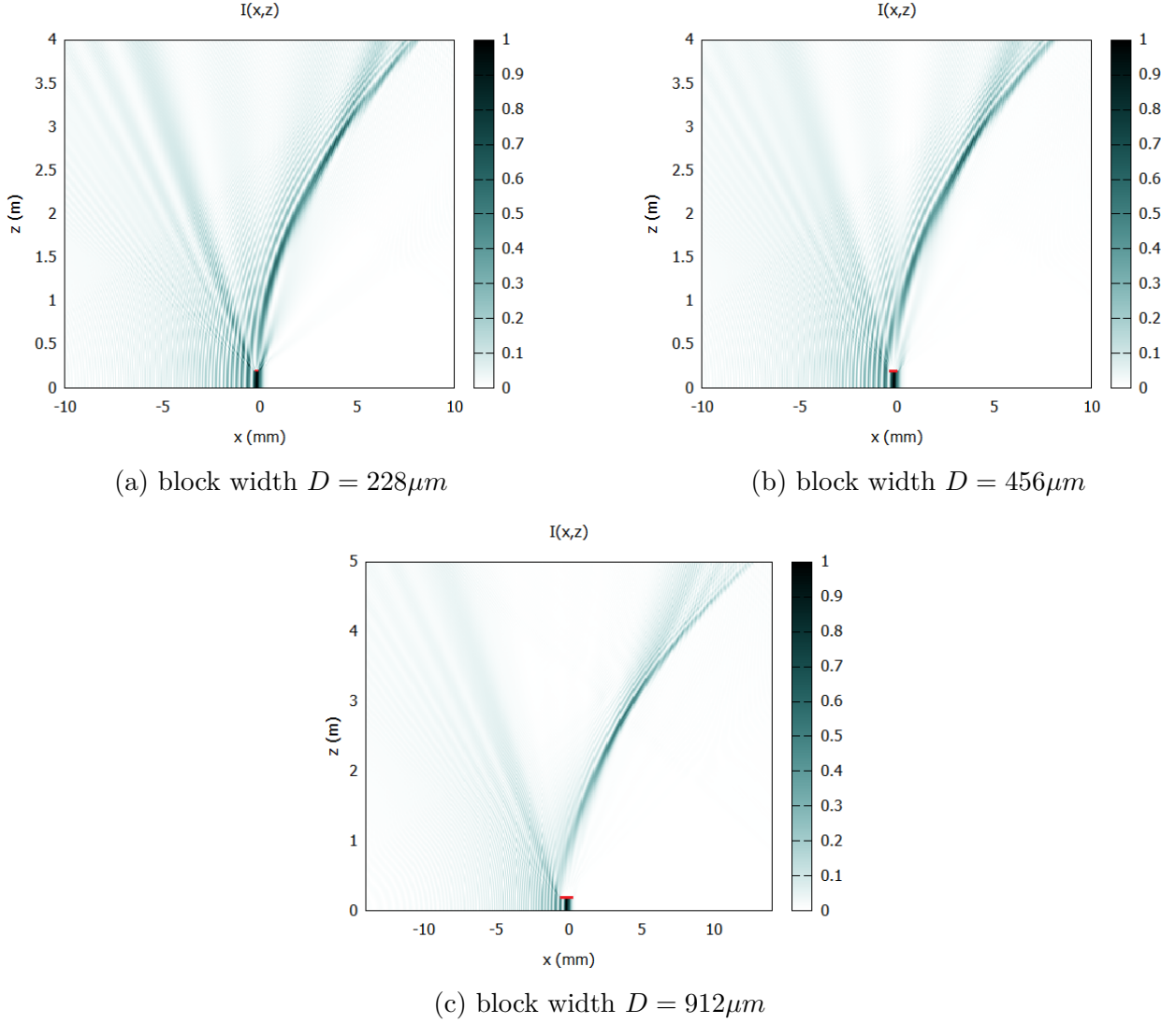
Figure 2.15: Self-reconstruction of one-dimensional Airy Beam with $\lambda = 800nm$, $w_g = 456\mu m$ that is intercepted by an obstacle of various widths D, placed at $z = 0.2m$, $x = -0.2mm$

At both Figures 2.14 and 2.15 we can observe that the one-dimensional Airy beam reconstructs after being intercepted by a block, at a propagation distance which is, approximately, the distance z_H that we calculated at Tables 7 and 8. The self - healing behaviour though, is not totally evident at Figures 2.14c and 2.15c. The reason for this is very simple. The typical distances of self-healing z_H for these configurations, $0.82m$ and $3.27m$, are greater than the corresponding Airy beam Rayleigh ranges z_r^{Ai}, that we find to be $0.65m$ and $2.61m$ respectively. That means that the beam can't fully self - reconstruct, since its main peak intensity has already dropped to lower than half of its initial value.

This observation gives us the opportunity to emphasize that we can refer to the one-dimensional Airy beams as truly non-diffracting, only if $a = 0$. For non-zero values of a, which is the only realistic situation, the one-dimensional Airy beams can be characterized as *pseudo non-diffracting* in the sense that they preserve the main properties of non-diffracting beams, such as self-healing, but only for propagation distances smaller than their Rayleigh range z_r^{Ai}.

Lastly, at this point we would like to make a comment about the characteristic scale of the propagation of an 1-D Airy Beam in z-axis. It is totally obvious from the Figures 2.14 and 2.15 that each propagation image of Figure 13 looks identical to the corresponding image of

Figure 14. That is because at each simulation configuration of Figure 14 we have used the corresponding configuration of Figure 13, with the changes: $w \to 2w$, $z_0 \to 4z_0$. The reason that leads to identical propagation images, is that the characteristic scale of propagation in z-axis is kw^2. That's why the dimensionless notation introduced in (2.10), $\xi = z/kw^2$, is very often preferred in the literature for describing the propagation of Airy beams.

Chapter 3

Ballistic dynamics of one-dimensional Airy beams

3.1 Introduction

In this chapter we wish to study the propagation of one-dimensional Airy beams to greater depth. We will deal with the amazing property of one-dimensional Airy beams to propagate in free space, following parabolic trajectories equivalent to those of a projectile moving under the action of a homogeneous gravitational field[21]. This behaviour allows them to bypass obstacles and optically reach any intended target. Our beginning will be, the one-dimensional paraxial wave equation (3.1).

$$i\frac{\partial u\left(x,z\right)}{\partial z} + \frac{1}{2k}\frac{\partial^2 u\left(x,z\right)}{\partial x^2} = 0 \qquad (3.1)$$

with the initial condition (2.2) **plus an initial tilt angle** θ described by an exponential phase factor $e^{ik\theta x}$:

$$u\left(x,0\right) = u_0 Ai\left(\frac{x}{w}\right)e^{a\frac{x}{w}}e^{ik\theta x} \qquad (3.2)$$

where, for simplicity, we have chosen the peak position of the primary lobe to be $x_0 = 0$. Solving (3.1) under the initial condition (3.2) leads to the following analytic expression for the beam's intensity $I(x,z)$:

$$I(x,z) = I_0 \left| Ai\left(\frac{x}{w} - \frac{z^2}{4k^2w^4} - \frac{\theta z}{w} + ia\frac{z}{kw^2}\right) \right|^2 e^{2a\frac{x}{w} - a\frac{z^2}{k^2w^4} - 2a\frac{\theta z}{w}} \qquad (3.3)$$

Under the assumption that $a \ll 1$, we can neglect the imaginary term of Airy' s argument and conclude to:

$$I(x,z) = I_0 \left| Ai\left(\frac{x}{w} - \frac{z^2}{4k^2w^4} - \frac{\theta z}{w}\right) \right|^2 e^{2a\frac{x}{w} - a\frac{z^2}{k^2w^4} - 2a\frac{\theta z}{w}} \qquad (3.4)$$

3.2 Ballistic propagation of the primary lobe

Using the argument of Airy function of equation (3.3), correspondingly to (2.2), we end up to the following expression for the transverse coordinate of the beam's primary peak:

$$x_{max}(z) = -w + \frac{1}{4k^2w^3}\cdot z^2 + \theta \cdot z \qquad (3.5)$$

It is easy to see that the primary lobe of the beam follows a parabola in $x-z$ plane, analogous with the trajectory of a projectile in a uniform gravitational field, where θ would be the

projectile's initial launch angle. We can also write the corresponding "Newtonian" kinematical equations:

$$g \equiv \frac{\partial^2 x_{max}}{\partial z^2}(z) = \frac{1}{2k^2w^3} \tag{3.6}$$

$$v(z) \equiv \frac{\partial x_{max}}{\partial z}(z) = \frac{z}{2k^2w^3} + \theta z = gz + \theta \tag{3.7}$$

where in our case g plays the role of gravitational acceleration, θ is the initial launch angle and z has taken the place of time t.

Before trying to numerically confirm that the beam's primary peak follows equation (3.5), we conduct some simulations using $Wp-Maxima$ in order to see the propagation images $I(x, z)$ of a beam whose initial field distribution is described by equation (3.2), with apodization factor $a = 0.02$, width parameter $w = 100$ μm and wavelength $\lambda = 8000$ nm, for various values of the tilt angle θ.

(a) $\theta = -0.24°$

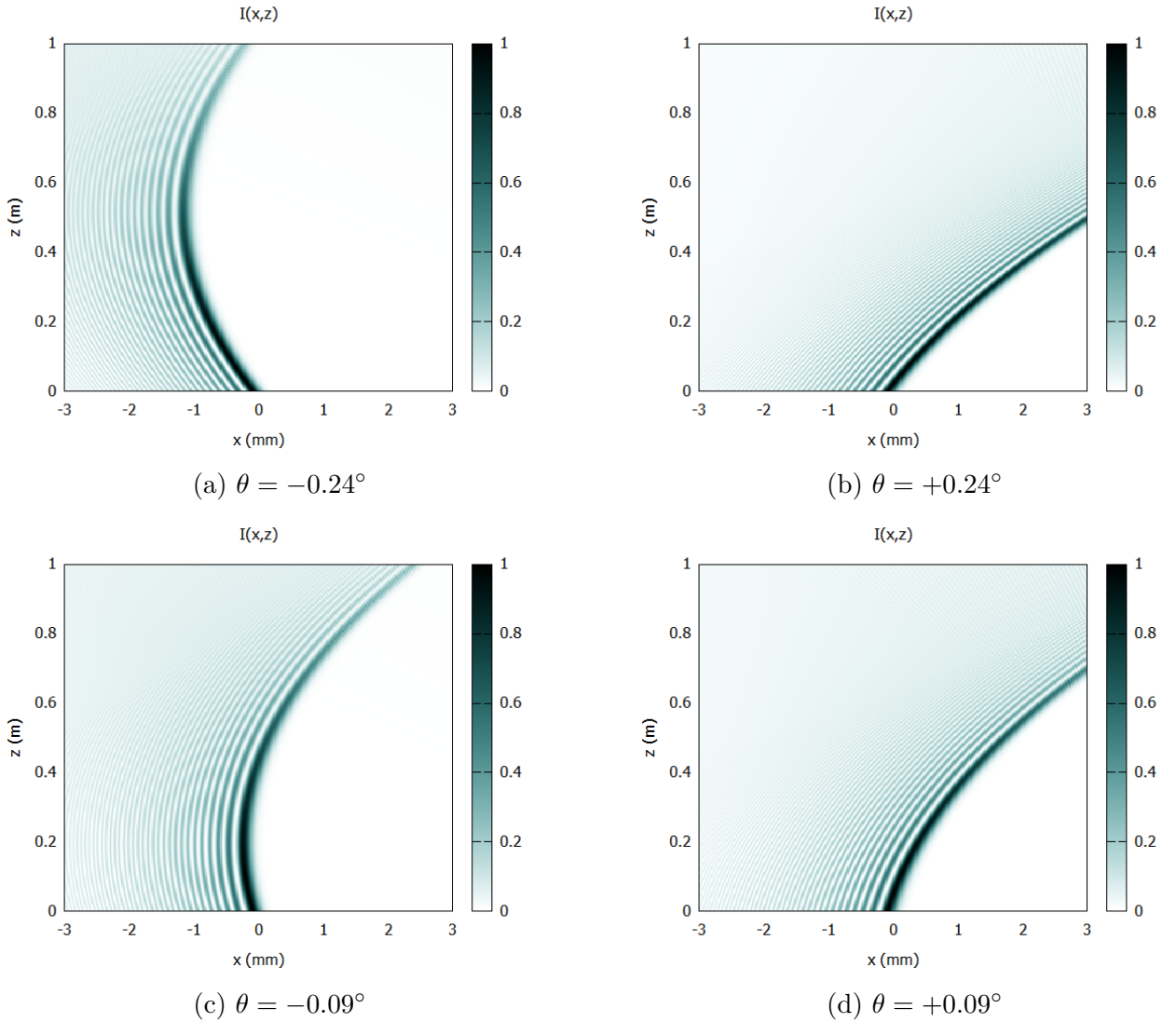(b) $\theta = +0.24°$

(c) $\theta = -0.09°$

(d) $\theta = +0.09°$

Figure 3.1: Intensity $I(x, z)$ profile of a propagating 1D Airy beam for various values of the tilt angle θ. (apodization factor $a = 0.02$, width parameter $w = 100$ μm and wavelength $\lambda = 800$ nm)

In Chapter 2, we have already confirmed numerically the validity of equation (3.5) for the case of $\theta = 0$. So, considering the dependence of x_{max} on the width parameter w and wavenumber k to be given by (3.5), we wish to confirm numerically that the dependence of x_{max} on z and θ (for non zero tilt angles θ) to be also given by (3.5).

In order to achieve that, we conduct numerical simulations using $Wp - Maxima$, as usual, for the propagation of an Airy beam at 1D+1 regime with wavelength $\lambda = 800$ nm, width parameter $w = 100$ μm and apodization factor $a = 0.05$.

We first ran a simulation with an initial launch angle $\theta = 0.07°$ and found the peak position x_{max} for various propagation distances z. In the following Table 9, we display our numerical results, compared to the corresponding theoretical predictions from equation (3.5).

Table 3.1

propagation distance	theoretical prediction	numerical calculation	difference
z(m)	x_{max}(mm)	x_{max}(mm)	(%)
0.1	0.063	0.075	19.0
0.2	0.306	0.322	5.2
0.3	0.631	0.639	1.3
0.4	1.037	1.053	1.5
0.5	1.524	1.547	1.6

At the following Figure 3.2, we have plotted in the same diagram the theoretical curve as predicted by (3.5) and the numerical results of the peak position x_{max} as a function of propagation distance z.
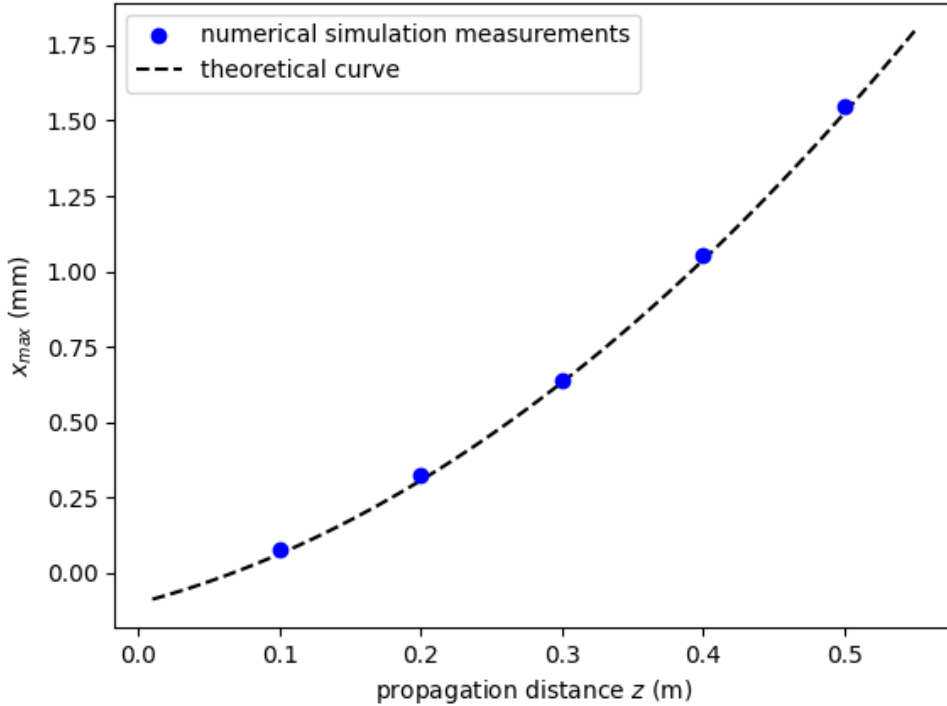

Figure 3.2: Airy primary lobe peak position as a function of the propagation distance

It is obvious from the previous diagram that the main lobe indeed moves in a parabola and that the numerical results are in excellent agreement with the theoretical relation.

Then, we ran numerical simulations using the same parameter values as previously, for different values of the initial launch angle θ and each time we found the main lobe transverse coordinate x_{max} for propagation distance $z = 0.2$ m. In Table 3.2 that follows, we display our numerical results, compared to the corresponding theoretical predictions from equation (3.5).

Table 3.2

initial tilt angle $\theta(°)$	theoretical prediction $x_{max}(\text{mm})$	numerical calculation $x_{max}(\text{mm})$	difference (%)
-0.5	-1.683	-1.675	0.5
-0.3	-0.999	-0.978	2.1
-0.1	-0.287	-0.288	-0.3
-0.07	-0.182	-0.172	5.5
-0.05	-0.112	-0.097	13.4
+0.05	0.237	0.247	4.2
+0.07	0.306	0.322	5.2
+0.1	0.411	0.429	4.4
+0.3	1.109	1.117	0.7
+0.5	1.807	1.810	0.2

In Fig. 3.3, we have plotted in the same diagram the theoretical curve as predicted by (3.5) and the numerical results of the peak position x_{max} for propagation distance $z = 0.2$ m as a function of the initial tilt angle θ.
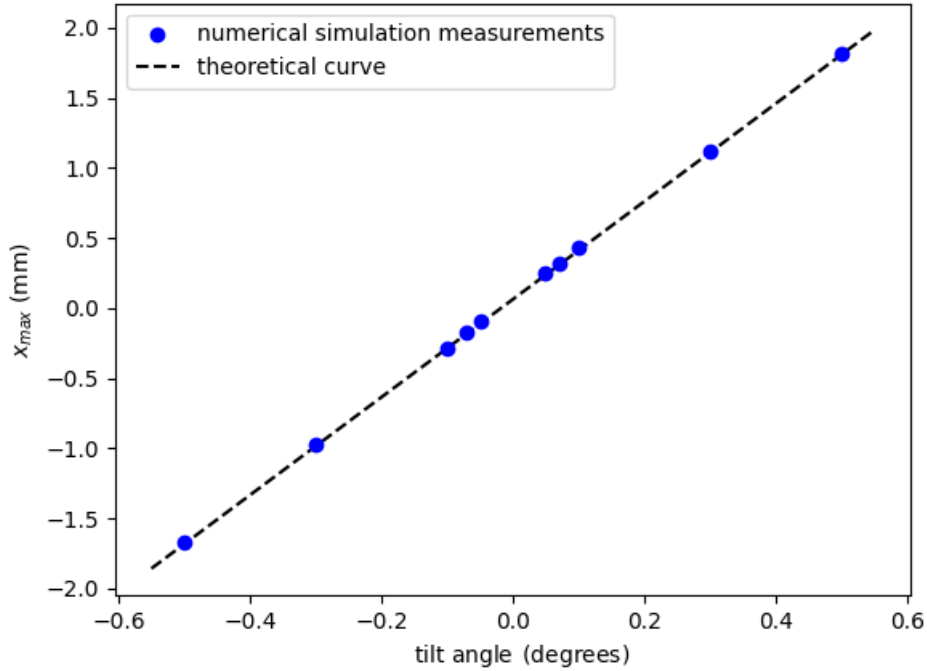

Figure 3.3: Airy primary lobe peak position at $z = 0.2$ m as a function of tilt angle θ.

We can conclude that the numerical measurements of the previous diagram are in excellent agreement with the theoretically expected values of the peak position $x_{max}(0.2$ m$)$ from equation (3.5).
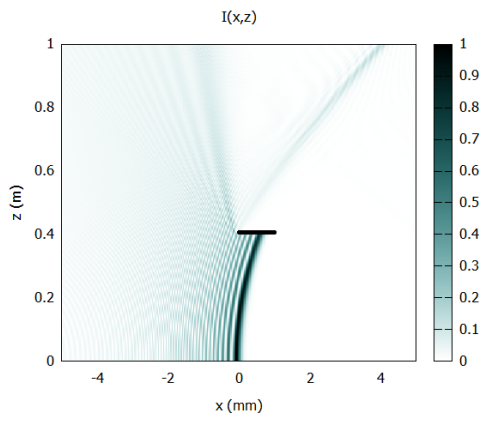
3.3   Bypassing an obstacle

At the previous subsection we numerically confirmed that the main lobe of an Airy Beam at 1D+1 regime follows a parabolic trajectory equivalent to that of a projectile in a homogeneous gravitational field. We now wish to take advantage of this interesting property in order to bypass obstacles and optically reach any wanted target.
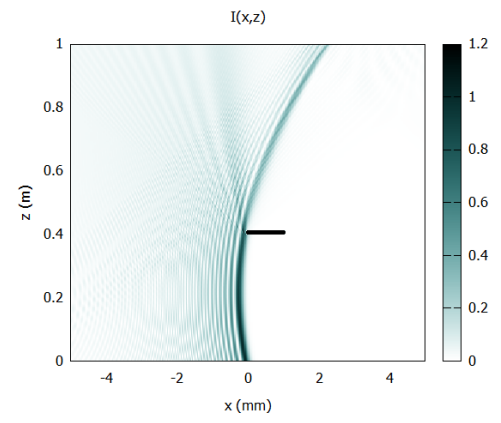
Let's suppose that we have a not-tilted Airy Beam, at 1D+1 regime, with apodization factor $a = 0.02$, width parameter $w = 100$ μm and wavelength $\lambda = 800$ nm, that propagates over z axis.

At first, an absorbing block of width $D = 1$ mm is placed at propagation distance $z = 0.4$ m with its center at transverse position $x = 0.4$ mm. This block does not allow the main lobe to continue its propagation (see Fig.3.4a). We will demonstrate the impressive ability of one-dimensional Airy beams to bypass obstacles at the following Figure 3.4b-3.4h, changing the initial launch angle of the beam and moving the block's position, as mentioned below.
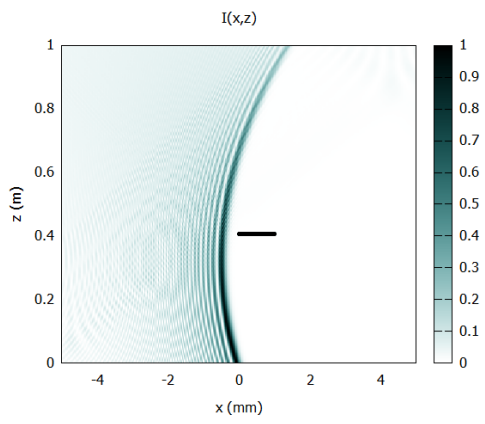
- We first set an initial launch angle at the Airy Beam, $\theta = -0.1°$. Although the main lobe is not totally destroyed by the block, it still does not bypass the obstacle (Fig.3.4b).

- Then, change the initial launch angle to $\theta = -0.15°$. *Now the obstacle is bypassed by the Airy Beam* (Fig.3.4c).

- The block's center is moved to transverse position $x = 0$ ((Fig.3.4d) and $x = -0.2mm$ (Fig.3.4e). Again the block intercepts the beam's propagation.

- We change the initial launch angle to $\theta = -0.25°$. *Again the obstacle is bypassed by the Airy Beam* (Fig.3.4f)

- The block's center is moved to transverse position $x = -1mm$ at propagation distance $z = 0.2m$ (Fig.3.4g). Again the obstacle blocks the beam's primary peak.

- Finally, we change the initial launch angle to $\theta = +0.15°$. Part of the beam is still blocked by the obstacle but the primary peak bypasses it and can optically reach any wanted target. (Fig.3.4h)
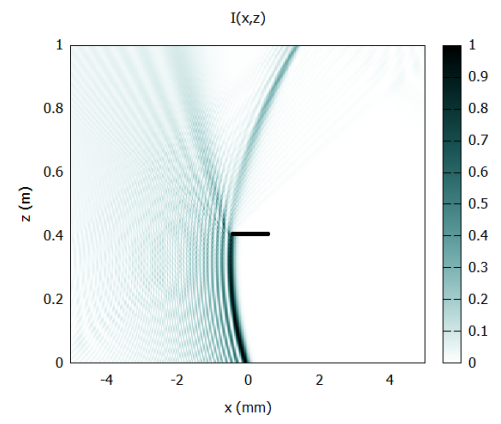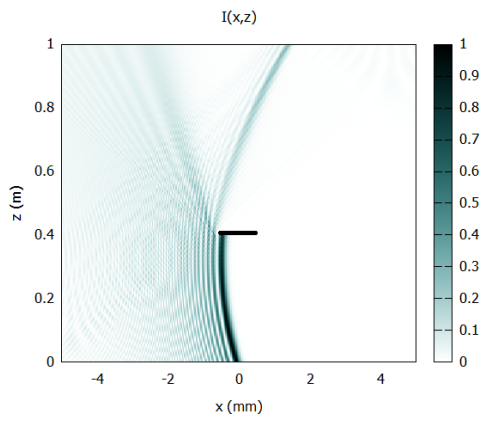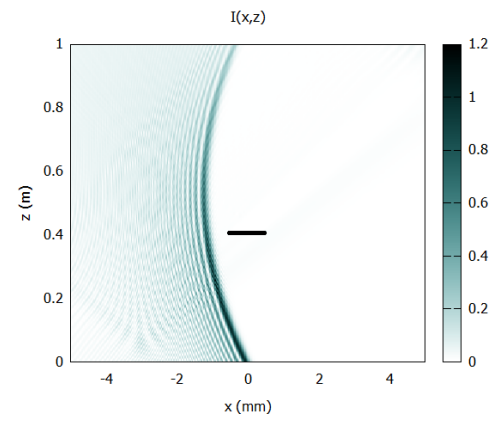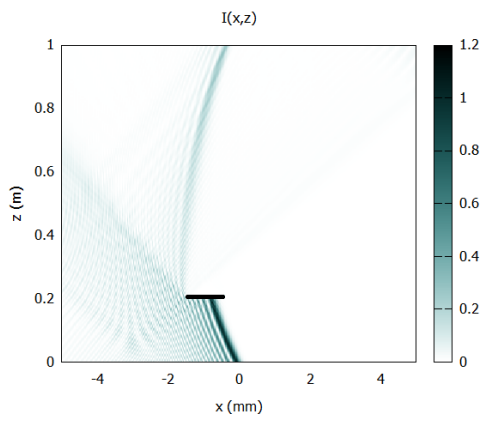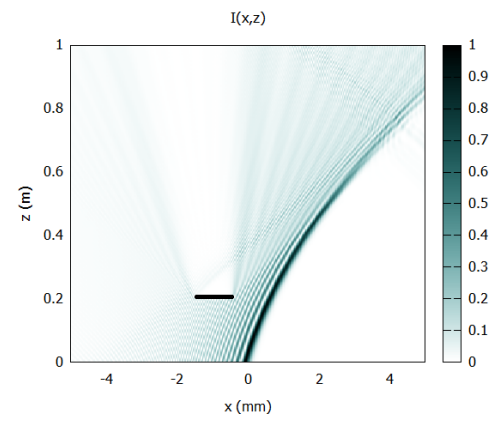
Figure 3.4: Optical obstacle bypassing

35

3.4 Superimposing one-dimensional Airy Beams

We will now study the propagation of an initial field distribution equivalent to two symmetric superimposing one-dimensional Airy Beams that accelerate at opposite directions. We will interestingly find out that this beam exhibits abrupt autofocusing [22], [23]. The initial field distribution has the form

$$u(x,0) = u_{Ai}(x,0) + u_{Ai}(-x,0) \tag{3.8}$$

where u_{Ai} is the usual field distribution of an Airy Beam at 1D+1 regime, i.e

$$u_{Ai}(x,0) = u_0 Ai\left(\frac{x+x_0}{w}\right)e^{a\frac{x+x_0}{w}} \tag{3.9}$$

where w, x_0 are respectively the primary lobe width and position parameters and a is the apodization factor. The primary peak x_L of the "left" Airy Beam $u_{Ai}(x,0)$ will propagate over z-axis following the equation of motion:

$$x_L(z) = -(x_0 + w) + \frac{z^2}{4k^2w^3} \tag{3.10}$$

whereas the primary peak of the "right" Airy Beam $u_{Ai}(-x,0)$, for obvious symmetry reasons, will follow the equation of motion:

$$x_R(z) = (x_0 + w) - \frac{z^2}{4k^2w^3} \tag{3.11}$$

While propagating over z-axis, the main lobes of the two symmetric Airy Beams will "collide" at some distance of propagation $z_0 \equiv f_{Ai}$, to which we will simply refer as *focal distance* f_{Ai}. Demanding from equations (3.10), (3.11) to obey the relation $x_L(f_{Ai}) = x_R(f_{Ai})$ we find theoretically that the two beams that accelerate at opposite directions focus, and their focus position is be given by:

$$f_{Ai} \cong 4\frac{\pi w^2}{\lambda}\sqrt{1 + \frac{x_0}{w}} \tag{3.12}$$

where the equality is absolutely valid only for small values of the apodization factor a. In order to confirm the validity of the above equation, we conducted numerical experiments using $Wp - Maxima$. At all our simulations, we chose to keep the apodization factor a constant to the value $a = 0.05$.

We demonstrate a typical propagation image of two symmetric superimposing Airy beams at 1D+1 regime, for wavelength $\lambda = 700nm$, peak position $x_0 = 0.5mm$ and $FWHM_{Ai} = 400\,\mu$m at the following Figure.
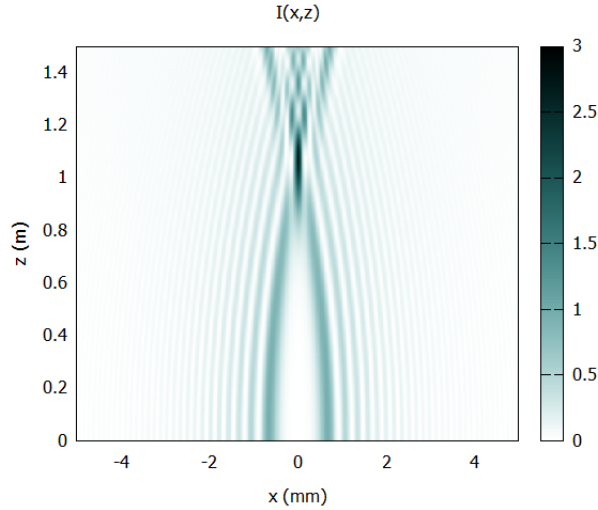
Figure 3.5: Intensity propagation image of two symmetric superimposing one-dimensional Airy beams.(peak position parameter $x_0 = 0.5$ mm and $FWHM_{Ai} = 400\mu$m

At first, we fixed the value of wavelength λ to $\lambda = 700$ nm, and the $FWHM_{Ai} \equiv w_g$ to $w_g = 400$ μm (so that the width parameter w was equal to $w = w_g/2.28 = 175.44$ μm) and changed the value of the peak position x_0. We ran numerical simulations altering the value of x_0 from $x_0 = 0.3$ mm to $x_0 = 0.7$ mm with 0.1 mm step, and each time we found the focus position f_{Ai}. In the following Table 3.3 we display our numerical results, compared to the corresponding theoretical predictions from equation (3.12).

Table 3.3

peak position parameter	theoretical prediction	numerical calculation	difference
x_0(mm)	f_{Ai}(m)	f_{Ai}(m)	(%)
0.3	0.9095	0.9087	-0.1
0.4	1.0006	0.9998	-0.1
0.5	1.0841	1.0831	-0.1
0.6	1.1616	1.1592	-0.2
0.7	1.2342	1.2281	-0.5

At the following Figure 3.6, we have plotted in the same diagram the theoretical curve as predicted by (3.12) and the numerical results of the focus position f_{Ai} as a function of the peak position x_0.
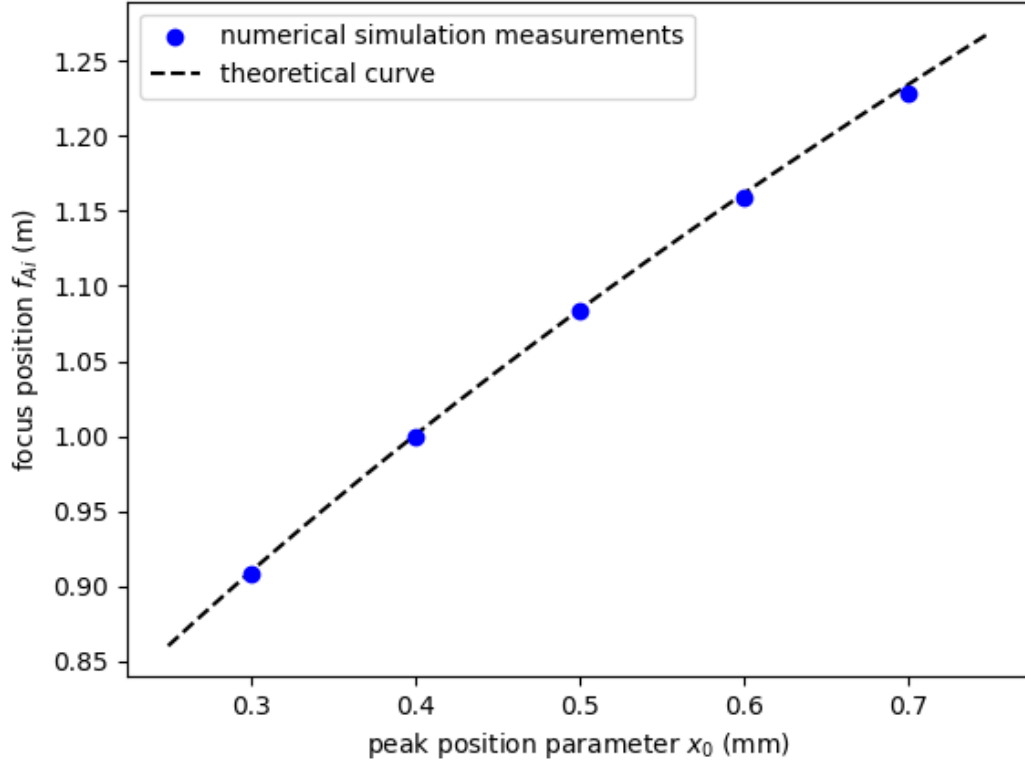
37

Figure 3.6

As we can see from this diagram, our numerical results are in very good agreement with the theoretical relation (3.12).

Then, we fixed the value of wavelength to $\lambda = 700$ nm and the peak position parameter to $x_0 = 0.5$ mm and changed the value of the width parameter w (by altering the corresponding value of $FWHM_{Ai} = 2.28w$). We ran numerical simulations altering the value of w from $w = 100$ μm to $w = 350$ μm with 50 μm step, and each time we found the focus position f_{Ai}. In the following Table 3.4 we display our numerical results, compared to the corresponding theoretical predictions from equation (3.12).

Table 3.4

width parameter	theoretical prediction	numerical calculation	difference
$w(\mu\text{m})$	$f_{Ai}(\text{m})$	$f_{Ai}(\text{m})$	$(\%)$
150	0.8408	0.8366	-0.5
200	1.3434	1.3408	-0.2
250	1.9434	1.9411	-0.1
300	2.6384	2.6302	-0.3
350	3.4271	3.4231	-0.1

At the following Figure 3.7, we have plotted in the same diagram the theoretical curve as predicted by (3.12) and the numerical results of the focus position f_{Ai} as a function of the width parameter w.
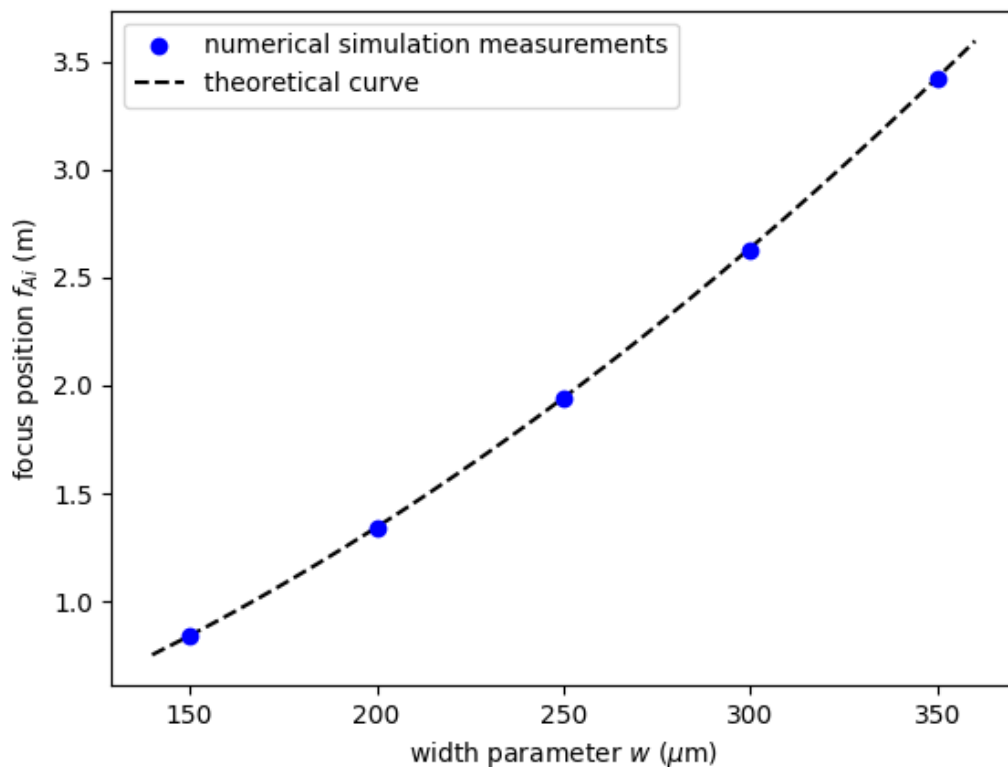
Figure 3.7: Focus position f_{Ai} as a function of the width parameter w.

As we can see from this diagram, our numerical results are in excellent agreement with the theoretical relation (3.12).

Lastly, we fixed the value of peak position x_0 to $x_0 = 0.5$mm and $FWHM$ to $FWHM_{Ai} = 400\mu$m changed the value of the wavelength λ. We ran numerical simulations altering the wavelength from $\lambda = 500\mu m$ to $w = 900\mu$m with 100μm step, and each time we found the focus position f_{Ai}. In the following Table 3.5 we display our numerical results, compared to the corresponding theoretical predictions from equation (3.12).

Table 3.5

wavelength	theoretical prediction	numerical calculation	difference
λ(nm)	f_{Ai}(m)	f_{Ai}(m)	(%)
500	1.5178	1.5159	-0.1
600	1.2648	1.2623	-0.2
700	1.0841	1.0829	-0.1
800	0.9486	0.9471	-0.2
900	0.8432	0.8417	-0.8

At the following Figure 3.8, we have plotted in the same diagram the theoretical curve as predicted by (3.12) and the numerical results of the focus position f_{Ai} as a function of the width parameter w.
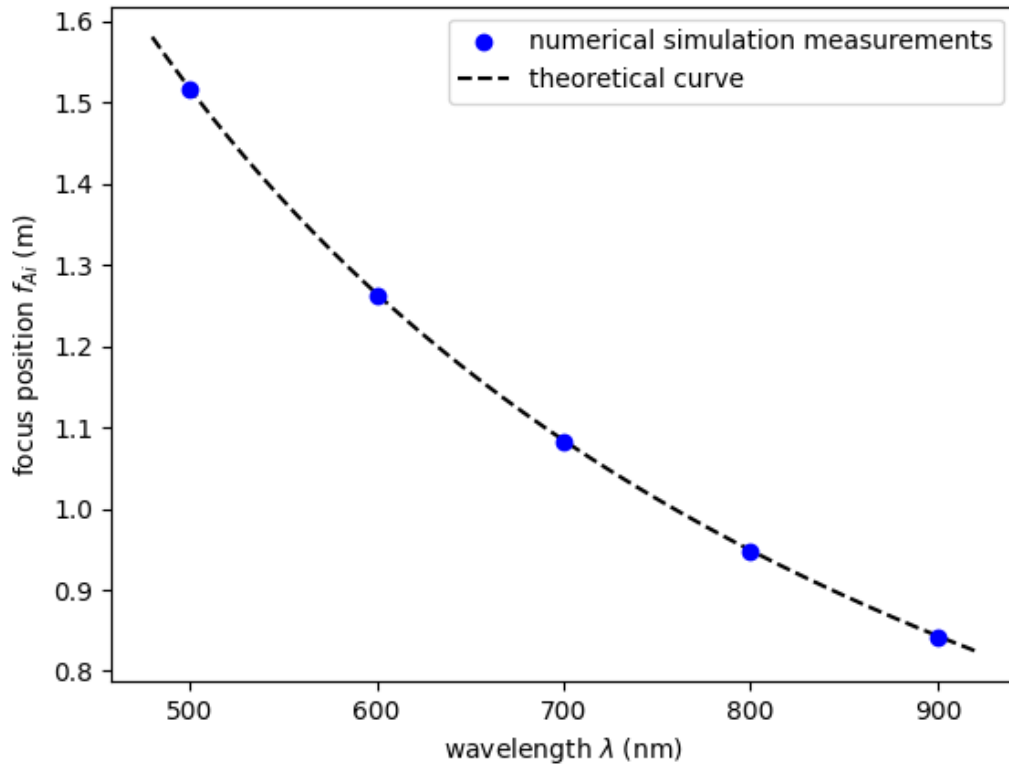
Figure 3.8: Focus position f_{Ai} as a function of the wavelength λ.

As we can see from this diagram, our numerical results are in excellent agreement with the theoretical relation (3.12).

Chapter 4

Janus Waves

4.1 Introduction: Conjugate and Janus Waves

As it was firstly noted by Papazoglou et al [24], there is a family of waves which are superposition of twin waves, conjugate to each other under inversion of the propagation direction. The two twin waves are related to the converging and diverging parts of the beam and are referred in the literature as "real" and "virtual" respectively. They can both be observed in the real space at two different foci positions if the beam is focused by a converging lens. We will theoretically study this family of waves.

Let's assume a harmonic wave whose electric field is given by $u(\vec{r}, z)$, where $\vec{r}$ is a vector that describes the transverse position and z is the propagation coordinate. We *define this wave as **conjugate wave*** if its field $u(\vec{r}, z)$ can be described as:

$$u(\vec{r}, z) = \psi(\vec{r}, z) + \psi^*(\vec{r}, -z) \tag{4.1}$$

i.e. as a superposition of two waves $\psi(\vec{r}, z)$ and $\psi^*(\vec{r}, z)$.

By simple observation, we find two obvious properties of a conjugate wave. Firstly, it is conjugate symmetric under inversion of the propagation direction, as:

$$u(\vec{r}, -z) = \psi(\vec{r}, -z) + \psi^*(\vec{r}, z) = (\psi^*(\vec{r}, -z))^* + (\psi(\vec{r}, z))^* = u^*(\vec{r}, z) \tag{4.2}$$

Furthermore, the field for $z = 0$ is always a real valued function, i.e.

$$u(\vec{r}, 0) = \psi(\vec{r}, 0) + \psi^*(\vec{r}, 0) = 2Re\left(\psi(\vec{r}, 0)\right) \tag{4.3}$$

This second property of conjugate waves motivates us to search for a mathematical criterion for characterizing a wave as *conjugate*. A sufficient condition for a wave to be conjugate, as was formulated by Papazoglou et al [24], [25], is the following:

Theorem 1. *If the field distribution $u(\vec{r}, z)$ of an harmonic wave is real valued at a transverse plane along its propagation, then the wave is conjugate.*

Proof. Without loss of generality, let's suppose that the field is real valued for $z = 0$, i.e $u(\vec{r}, 0) = Re\left(u(\vec{r}, 0)\right)$. The angular spectrum [7] $P(k_x, k_y; z = 0) \equiv P_0(k_x, k_y) \equiv P_0(\vec{k_\perp})$ of this real valued field is given by:

$$P_0(\vec{k_\perp}) = \iint u(x, y, 0)e^{-i(k_x x + k_y y)}\, dx\, dy \tag{4.4}$$

where $\vec{k_\perp}$ are the transverse components of the wavevector. We can easily show that the function $P_0(\vec{k_\perp})$ is hermitian, $P_0(-\vec{k}_\perp) = P_0^*(\vec{k_\perp})$:

$$P_0(-\vec{k_\perp}) = \iint u(x, y, 0)e^{i(k_x x + k_y y)}\, dx\, dy = P_0^*(\vec{k_\perp}) \tag{4.5}$$

so that we can describe it as:

$$P_0(\vec{k_\perp}) = \left| P_0(\vec{k_\perp}) \right| e^{i\phi_0(\vec{k_\perp})} \tag{4.6}$$

where the magnitude $\left| P_0(\vec{k_\perp}) \right|$ and the argument $\phi_0(\vec{k_\perp})$ are even and odd functions, respectively, of the transverse component $\vec{k_\perp}$ of the wavevector.

The field distribution at some distance z along the propagation axis can now be expressed [7, 24] as:

$$u(\vec{r}, z) = \iint \left| P_0(\vec{k_\perp}) \right| e^{i\phi_0(\vec{k_\perp})} e^{iz\sqrt{k_0^2 - k_\perp^2}} e^{i(k_x x + k_y y)} dk_x \, dk_y \tag{4.7}$$

Setting:

$$\psi(\vec{r}, z) = \frac{1}{2} \iint \left| P_0(\vec{k_\perp}) \right| e^{i\phi_0(\vec{k_\perp})} e^{iz\sqrt{k_0^2 - k_\perp^2}} e^{i(k_x x + k_y y)} dk_x \, dk_y \tag{4.8}$$

we easily conclude that the field distribution can be expressed as:

$$u(\vec{r}, z) = \psi(\vec{r}, z) + \psi^*(\vec{r}, -z) \tag{4.9}$$

∎

From the large variety of conjugate waves that satisfy this criterion, we are interested in studying the properties of those that exhibit a discrete focus away from their symmetry plane. We refer to these waves as *Janus Waves* [24].

4.2   Janus Waves focusing using Matrix theory

In this subsection, our aim is to theoretically predict the effect of the presence of a lens on the propagation of an auto-focusing beam that belongs to the family of Janus Waves [24], such as the superposition of two symmetric 1D Airy beams that we discussed in Section 3.4. We will prefer, at first, to study the effect of the presence of a general imaging system on the propagation of a general auto-focusing beam, under the geometrical optics approximation [25].

Let's suppose that we have an auto-focusing beam that propagates in free space. This beam propagates in a way that local maxima are generated along the propagation axis. In the context of geometrical optics, that means that many light rays intersect at the maxima positions.

Now, let's suppose an optical system with principal planes H and H' and a light ray that intersects the entrance principal plane H at height h with inclination α. If the optical system was absent, the ray would intersect the propagation axis z at some position with distance $z_0 = \frac{|h|}{\alpha}$ from the plane H.

The effect of the optical system on the propagation of this ray can be easily found if we use the general optical system (with principal planes H, H') $ABCD$ matrix representation, i.e

$$M = \begin{pmatrix} 1 & 0 \\ -P & 1 \end{pmatrix} \tag{4.10}$$

where P is the optical power of the system. Actually, if we denote with n and n' the refractive indices of the media before and after the optical system, respectively, then the height h' and the inclination α' of the ray at the exit principal plane H' will be given by:

$$\begin{pmatrix} h' \\ n'\alpha' \end{pmatrix} = \begin{pmatrix} 1 & 0 \\ -P & 1 \end{pmatrix} \begin{pmatrix} -|h| \\ n\alpha \end{pmatrix} = \begin{pmatrix} -|h| \\ Ph + n\alpha \end{pmatrix} \tag{4.11}$$

Thus, the intersection coordinate z_1 of the optical ray with the propagation axis(measured from the exit principal plane H'), with the presence of the optical system, will be:

$$z_1 = \frac{|h'|}{\alpha'} = \frac{n'\,|h|}{Ph + n\alpha} = \frac{|h|}{\alpha}\frac{n'}{P \cdot \frac{|h|}{\alpha} + n} = z_0\frac{n'}{Pz_0 + n} \tag{4.12}$$

From the previous equation, we conclude that:

$$\frac{n}{-z_0} + \frac{n'}{z_1} = P \tag{4.13}$$

The last equation has the general form of the relation between the object position, $s \leftrightarrow -z_0$, and the image position, $s' \leftrightarrow z_1$, of an optical system with optical power P. This correspondence is totally reasonable. Firstly, the focus without the presence of the optical system corresponds to the object, which is located after the entrance of the optical system and, thus, is imaginary($s < 0$). Then, the focus after the presence of the optical system corresponds to the image, which is located after the exit of the optical system and thus is real ($s' > 0$).

In our case, the optical system is just a thin converging lens($P = \frac{1}{f}$) and the surrounding medium is air ($n = n' = 1$), so that the equation (3.12) is reduced to:

$$\frac{1}{-z_0} + \frac{1}{z_1} = \frac{1}{f} \tag{4.14}$$

and the principal planes H and H' coincide, at $z = 0$. Our beam of interest has the initial field distribution introduced in eq. (3.8), and belongs to the family of *Janus Waves*, because it is a *Conjugate Wave* ($u(x,0) \in \mathbb{R}$) and is auto-focusing, as we saw in Section 3.4. This beam will abruptly autofocus at a distance $z_0 \equiv f_{Ai}$ along the propagation direction, but, since is Conjugate, will also have a conjugate focus at position $-z_0 = -f_{Ai}$ which is not physically accessible when the beam propagates in free space.

Thus, after the addition of the thin lens, we expect that the initial "real" focus will be imaged to a position z that satisfies the equation [24]:

$$\frac{1}{z} - \frac{1}{f_{Ai}} = \frac{1}{f} \tag{4.15}$$

and, analogously, the "virtual" focus will be imaged to a position z that satisfies the equation [24]:

$$\frac{1}{z} + \frac{1}{f_{Ai}} = \frac{1}{f} \tag{4.16}$$

4.3   Double foci positions

At the previous subsection, we found the following theoretical relation for the double foci positions z of the two symmetric one-dimensional Airy Beams after they are focused by a lens of focal length f:

$$\frac{1}{z} \pm \frac{1}{f_{Ai}} = \frac{1}{f} \tag{4.17}$$

where with f_{Ai} we denote the focus position of the two symmetric superimposing Airy Beams at 1D+1 regime, without the presence of the focusing lens. Thus, eq. (4.17) leads to two foci, with positions z_1 and z_2 given by:

$$z_1 = \frac{f \cdot f_{Ai}}{f + f_{Ai}} \tag{4.18}$$

and

$$z_2 = \frac{f \cdot f_{Ai}}{f_{Ai} - f} \tag{4.19}$$

Recalling that the initial focus position f_{Ai} is a function of the width parameter w and the peak position x_0 of the one-dimensional Airy Beams, i.e

$$f_{Ai} = 4\frac{\pi w^2}{\lambda}\sqrt{1 + \frac{x_0}{w}} \tag{4.20}$$

we will try to numerically confirm the validity of equations (4.18), (4.19) for the two foci positions by altering the width parameter w, the peak position x_0 and the focal length f, while keeping the wavelength constant to $\lambda = 800$ nm.

At first, we fixed the focal length f to $f = 0.6$ m and the value of peak position x_0 to $x_0 = 5 \cdot 10^{-4}$ m and changed the value of the width parameter w(by altering the beam's $FWHM_{Ai}$, as $FWHM_{Ai} = 2.28w$). We ran numerical simulations altering the value of $FWHM_{Ai}$ from $FWHM_{Ai} = 500$ μm to $FWHM_{Ai} = 1300$ μm with 200 μm step, and each time we found the two foci positions z_1 and z_2. In the following Table 4.1 we display our numerical results, compared to the corresponding theoretical predictions from equations (4.18), (4.19).

Table 4.1

$FWHM_{Ai}$ (μm)	z_1 theoretical prediction(m)	z_1 numerical calculation(m)	z_2 theoretical prediction(m)	z_2 numerical calculation(m)
500	0.4171	0.42	1.069	1.04
700	0.4800	0.48	0.7999	0.8011
900	0.5160	0.51	0.7167	0.7256
1100	0.5381	0.5311	0.6780	0.6922
1300	0.5526	0.5467	0.6563	0.6622

We demonstrate the intensity propagation images, for the cases $FWHM_{Ai} = 500\mu m$ and $FWHM_{Ai} = 1300\mu m$, together with attached colourbars that correspond to the intensity, at the following Figure 21.

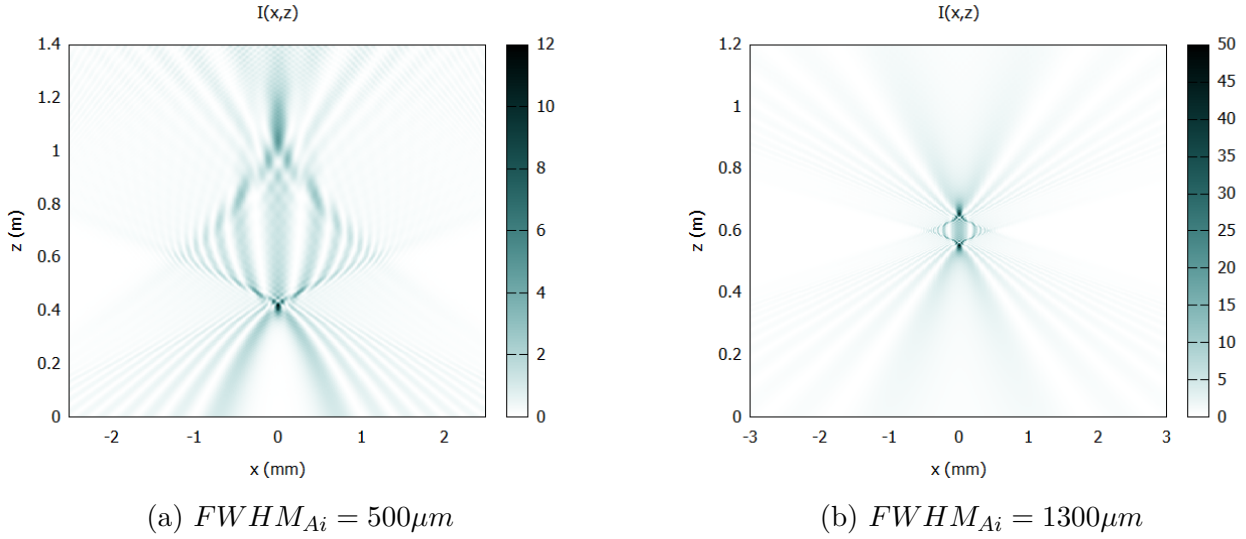(a) $FWHM_{Ai} = 500 \mu m$ (b) $FWHM_{Ai} = 1300 \mu m$

Figure 4.1: Intensity propagation images, for two symmetric superimposing 1D Airy Beams that are focused by a lens of $f = 0.6$ m. ($\lambda = 800$ nm, $x_0 = 5 \cdot 10^{-4}$ m for different values of $FWHM_{Ai}$

At the following Figure 4.2, we have plotted in the same diagram the theoretical curves as predicted by (4.18) and (4.19) and the numerical results of the focus positions z_1, z_2 as functions of the $FWHM_{Ai}$.
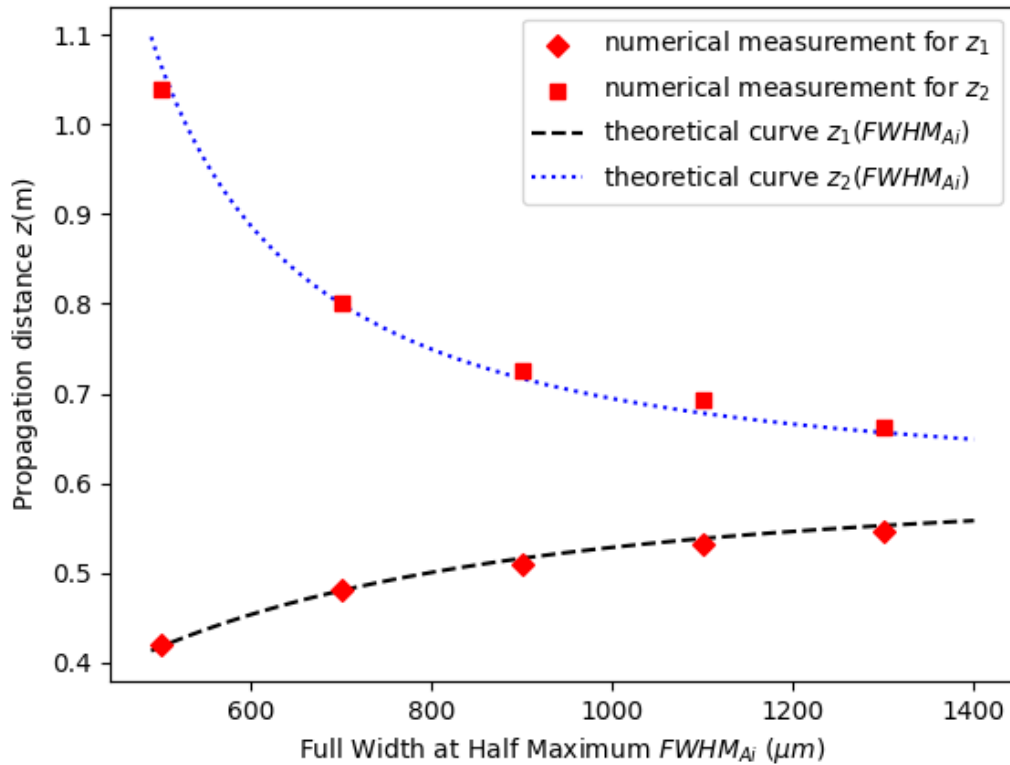

Figure 4.2

It is obvious that our numerical results are in very good agreement with the theoretical prediction.

Next, we kept the focal length fixed to $f = 0.6$ m and the width parameter to $w = 219.29$ μm(so that the $FWHM_{Ai}$ was equal to $FWHM_{Ai} = 500$ μm), and changed the peak position x_0. We ran numerical simulations altering the value of x_0 in a range between $x_0 = 5 \cdot 10^{-4}$ m to $x_0 = 20 \cdot 10^{-4}$ m, and each time we found the two foci positions z_1 and z_2. In the following Table 4.2 we display our numerical results, compared to the corresponding theoretical predictions from equations (4.18) and (4.19).

Table 4.2

x_0 $(10^{-4}m)$	z_1 theoretical prediction(m)	z_1 numerical calculation(m)	z_2 theoretical prediction(m)	z_2 numerical calculation(m)
5	1.0687	1.04	0.4171	0.42
7.5	0.9643	0.9806	0.4355	0.4306
10	0.9048	0.8971	0.4488	0.45
15	0.8376	0.8357	0.4674	0.4686
20	0.7997	0.8029	0.4801	0.4786

At the following Figure 4.3, we have plotted in the same diagram the theoretical curves as predicted by (4.18) and (4.19) and the numerical results of the focus positions z_1, z_2 as functions of the peak position x_0.
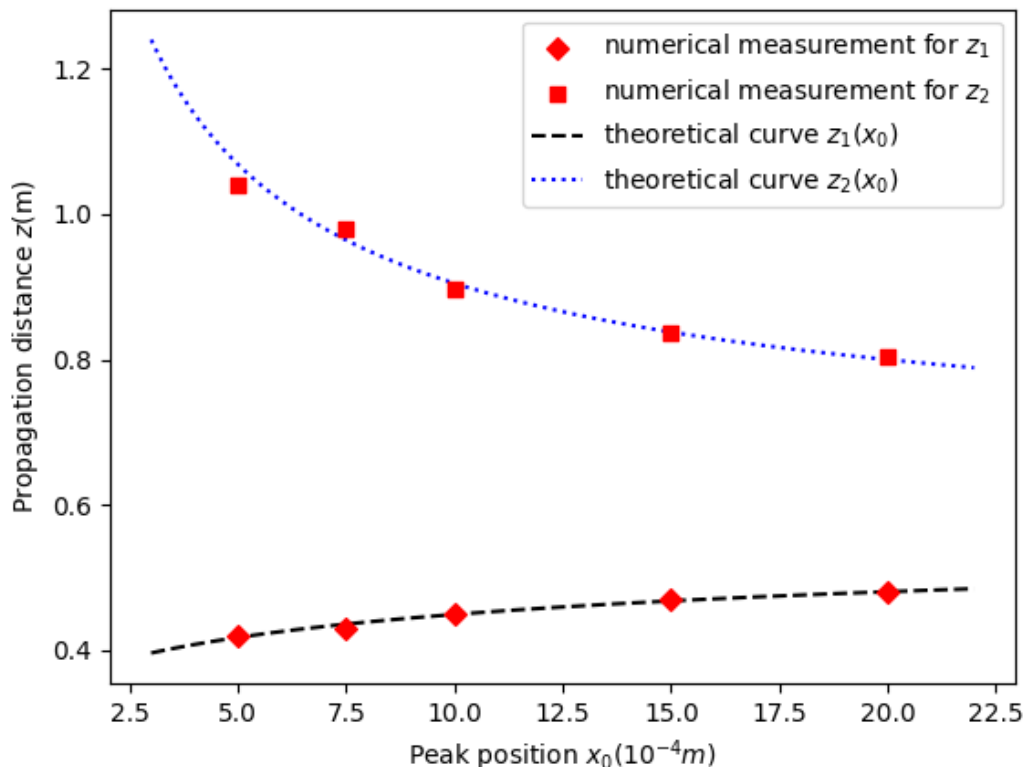

Figure 4.3

Again, we see that our numerical results are in very good agreement with the theoretical prediction.

Finally, we kept the peak position fixed to $x_0 = 15 \cdot 10^{-4}$ m and the width parameter to $w = 219.29$ μm(so that the $FWHM_{Ai}$ was equal to $FWHM_{Ai} = 500$ μm), and changed the

focal length of the lens f. We ran numerical simulations altering the value of f from $f = 0.4$ m to $f = 1.2$ m with a step of 0.2 m, and each time we found the two foci positions z_1 and z_2. In the following Table 4.3 we display our numerical results, compared to the corresponding theoretical predictions from equations 3.2.

<div align="center">Table 4.3</div>

$f(m)$	z_1 theoretical prediction(m)	z_1 numerical calculation(m)	z_2 theoretical prediction(m)	z_2 numerical calculation(m)
0.4	0.4933	0.4921	0.3364	0.335
0.6	0.8376	0.8357	0.4674	0.4686
0.8	1.2866	1.279	0.5805	0.5807
1.0	1.8967	1.897	0.6789	0.68
1.2	2.7735	2.7709	0.7656	0.7622

At the following Figure 4.4, we have plotted in the same diagram the theoretical curves as predicted by (4.18) and (4.19) and the numerical results of the focus positions z_1, z_2 as functions of the focal length f.
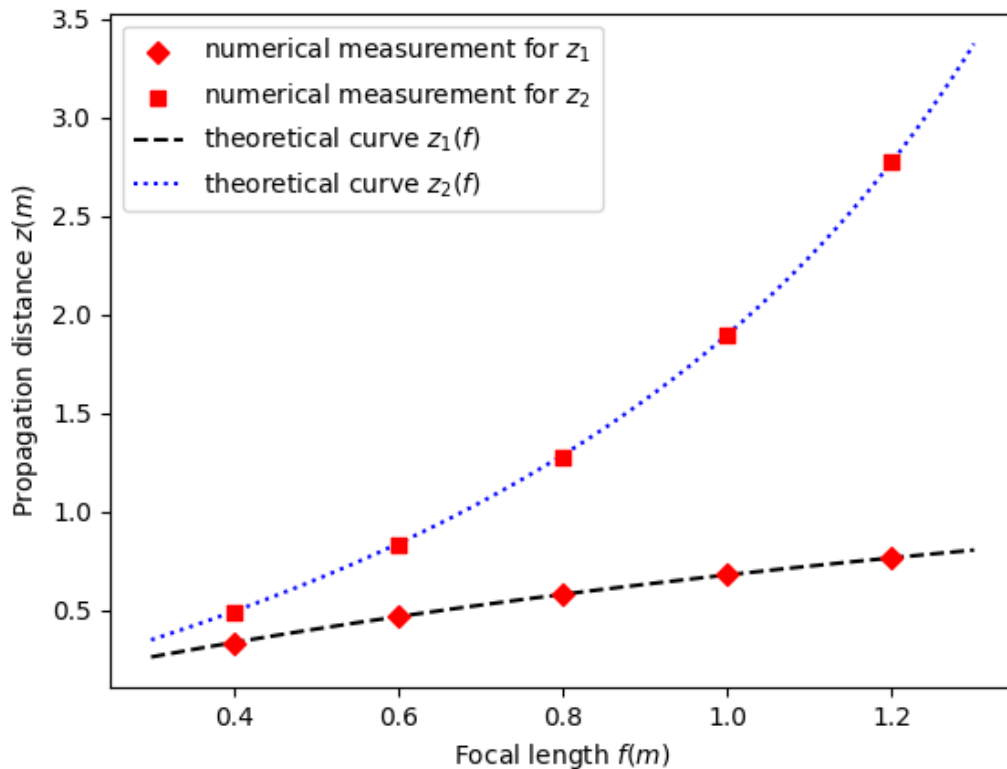

<div align="center">Figure 4.4</div>

Again, we see that our numerical results are in excellent agreement with the theoretical prediction.

4.4 Focusing by an axicon

After studying the propagation of two symmetric 1D Airy Beams that are focused by a converging lens, we wish to find out the behaviour of these beams when the converging lens is replaced by a plano-convex *axicon* [26].

An axicon is a specialized type of refractive optical element which has a conical surface. It is widely used in order to convert a Gaussian beam into a non-diffractive *Bessel*-like beam by adding a conical phase gradient to the initial beam. This is schematically shown in the Fig. 4.5.
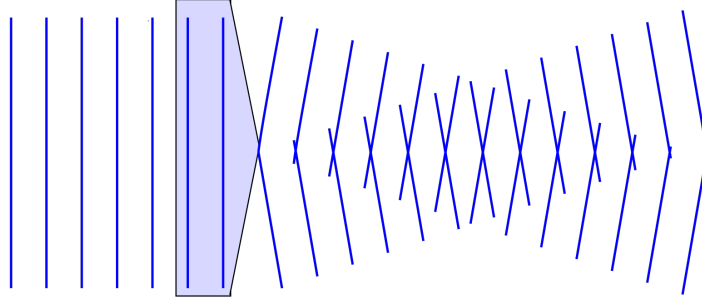

Figure 4.5: Diagram of Axicon and resulting Bessel Beam, Wiki

In the case of symmetric one-dimensional Airy beams, the action of an 1D axicon of cone angle θ is equivalent to a prism that leads to the addition of an initial tilt angle of opposite sign for each of the two symmetric Airy beams. So, the field distribution after the presence of the 1D axicon for the "left" Airy Beam will be:

$$u_L(x, 0) = u_0 Ai\left(\frac{x + x_0}{w}\right) e^{a\frac{x+x_0}{w}} e^{ik\theta x} \tag{4.21}$$

Respectively, the field distribution after the presence of the 1D axicon for the "right" Airy Beam will be

$$u_R(-x, 0) = u_0 Ai\left(\frac{-x + x_0}{w}\right) e^{a\frac{-x+x_0}{w}} e^{-ik\theta x} \tag{4.22}$$

We can easily conclude that the equations of motion of the "left" and "right" Airy beams' primary lobes after passing through an 1D axicon of cone angle θ will be, respectively [26]:

$$x_L(z) = -(x_0 + w) + \frac{z^2}{4k^2w^3} + \theta \cdot z \tag{4.23}$$

$$x_R(z) = (x_0 + w) - \frac{z^2}{4k^2w^3} - \theta \cdot z \tag{4.24}$$

Now, it is trivial to find the focus position of this field distribution at the propagation axis, simply demanding from equations (4.23) and (4.24) to obey the relation $x_L(z) = x_R(z)$.

Solving the resulting quadratic equation we end up to the following relation for the focus position:

$$z_\pm = \frac{4\pi w^2}{\lambda}\left[-\frac{2\pi w\theta}{\lambda} \pm \sqrt{\frac{4\pi^2 w^2\theta^2}{\lambda^2} + \left(\frac{x_0}{w}+1\right)}\right] \tag{4.25}$$

It is often preferred in the literature [26] to introduce the notation $z_{Ai} = kw^2/2$, $\tilde{x} = x_0/w + 1$ (normalised position parameter), $\tilde{\theta} = z_{Ai}\theta/w$ (normalized cone angle), so that the previous equation takes the simpler form

$$z_\pm = 4z_{Ai}\left[-2\tilde{\theta} \pm \sqrt{4\tilde{\theta}^2 + \tilde{x}}\right] \tag{4.26}$$

Of course, the positive solution z_+ corresponds to a real focus and we will refer to it simply as *focus position* $f_{Ax} \equiv z_+$. On the other hand, the negative solution z_- corresponds to a virtual focus, and is not visible without the presence of a converging lens. So, we finally have the following expression for the focus position f_{Ax}:

$$f_{Ax} = \frac{4\pi w^2}{\lambda}\left[-\frac{2\pi w\theta}{\lambda} + \sqrt{\frac{4\pi^2 w^2\theta^2}{\lambda^2} + \left(\frac{x_0}{w}+1\right)}\right] \tag{4.27}$$

Having derived an analytical expression for the focus position f_{Ax}, we will try to confirm it numerically, conducting simulations with $Wp - Maxima$, as usual. At first, we conduct a numerical experiment in order to see the propagation image of two symmetric superimposing one-dimensional Airy beams with wavelength $\lambda = 800nm$, peak position $x_0 = 15 \cdot 10^{-4}$ m, $FWHM_{Ai} = 500$ μm and apodization factor $a = 0.02$, *that are focused by an 1D axicon* of cone angle $\theta = 0.03°$. We demonstrate the propagation of this configuration in Fig. 4.6.
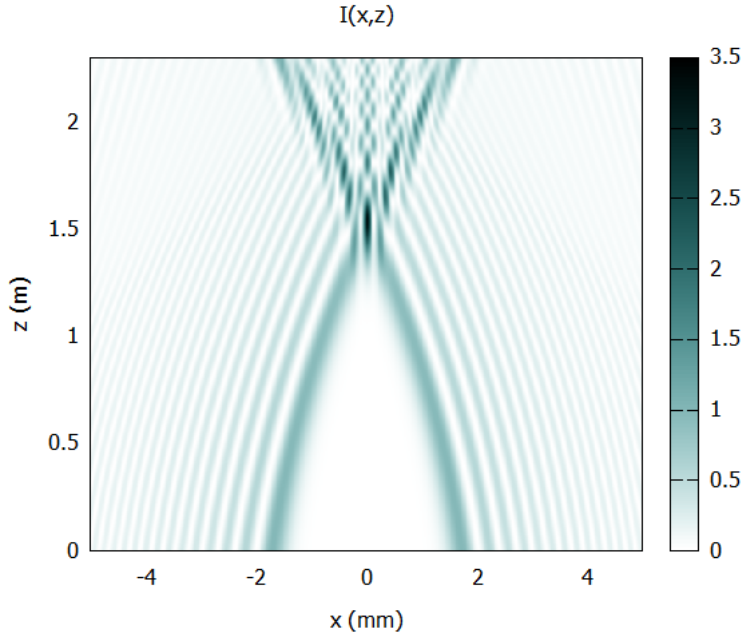

Figure 4.6: propagation of two symmetric 1D Airy beams with $\lambda = 800nm$, $x_0 = 15 \cdot 10^{-4}m$, $FWHM_{Ai} = 500\mu m$ and $a = 0.02$, *that are focused by an axicon of $\theta = 0.03°$*

It is clear from the previous figure that the two beams indeed focus at some propagation distance. Now we will try to confirm the validity of the analytical relation (4.27).

We will try to numerically confirm the validity of equation (4.27) for the focus position by altering the wavelength λ, the peak position x_0 and the axicon's cone angle θ, while keeping the $FWHM_{Ai}$ constant to $FWHM_{Ai} = 500$ μm)(and thus the width parameter constant to $w = 219.29\mu m$).

At first, we fixed the axicon's cone angle θ to $\theta = 0.03°$ and the peak position x_0 to $x_0 = 15 \cdot 10^{-4}$ m and changed the value of the wavelength λ. We ran numerical simulations altering the value of λ from $\lambda = 500nm$ to $\lambda = 900$ nm with 100 nm step, and each time we found the focus position f_{Ax}. In the following Table 4.4 we display our numerical results, compared to the corresponding theoretical prediction from Eq. 3.11.

Table 4.4

wavelength	theoretical prediction	numerical calculation	difference
λ(nm)	f_{Ax}(m)	f_{Ax}(m)	(%)
500	2.063	2.058	0.2
600	1.858	1.866	0.4
700	1.686	1.692	0.4
800	1.541	1.528	0.8
900	1.417	1.416	0.1

In Fig. 4.7, we have plotted in the same diagram the theoretical curve as predicted by (4.27) and the numerical results of the focus positions f_{Ax} as a function of the wavelength λ.
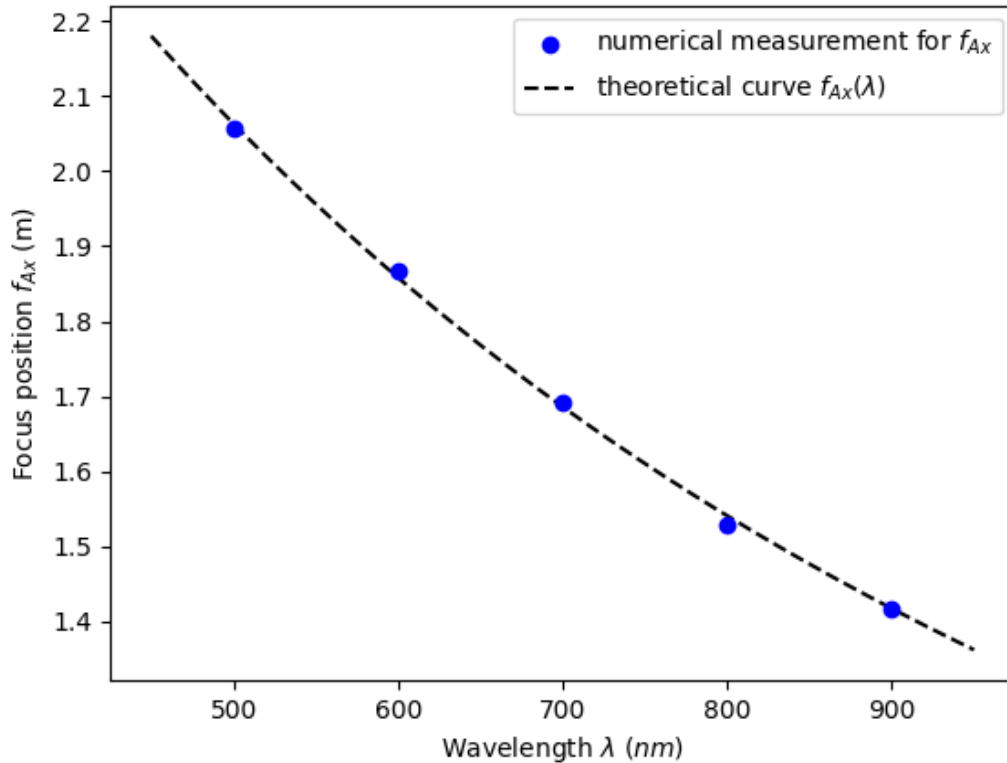

Figure 4.7: Focus position f_{Ax} as a function of the wavelegth λ

It is clear from the previous diagram that our numerical results are in very good agreement with the theoretical prediction.

Subsequently, we fixed the axicon's cone angle θ to $\theta = 0.03°$ and the wavelength λ to $\lambda = 900$ nm and changed the value of the peak position x_0. We ran numerical simulations altering the value of x_0 from $x_0 = 5 \cdot 10^{-4}$ m to $x_0 = 25 \cdot 10^{-4}$ m with $5 \cdot 10^{-4}$ m step, and each time we found the focus position f_{Ax}. In Table 4.5 we display our numerical results, compared to the corresponding theoretical prediction from Eq. (4.27).

Table 4.5

peak position $x_0(10^{-4}\text{m})$	theoretical prediction $f_{Ax}(\text{m})$	numerical calculation $f_{Ax}(\text{m})$	difference $(\%)$
5	0.792	0.792	0.0
10	1.134	1.134	0.0
15	1.417	1.416	0.1
20	1.665	1.668	0.2
25	1.887	1.880	0.4

Likewise in Fig. 4.8, we have plotted in the same diagram the theoretical curve as predicted by (4.27) and the numerical results of the focus positions f_{Ax} as a function of the peak position x_0.
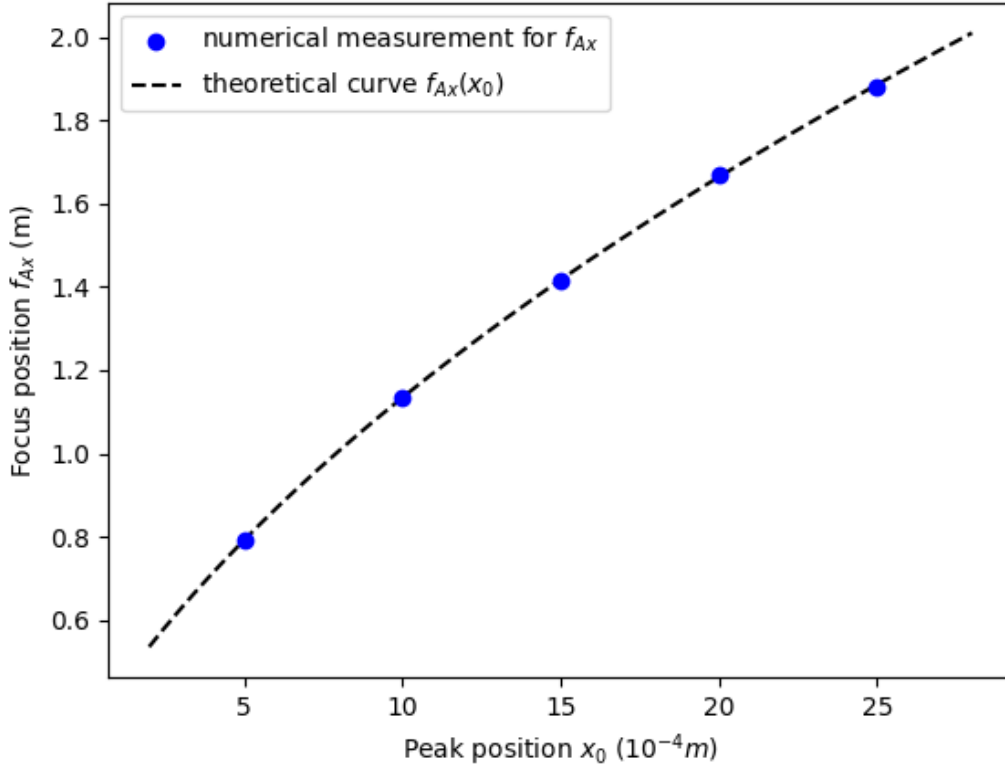

Figure 4.8: Focus position f_{Ax} as a function of the peak position parameter x_0

Again, it is clear from the previous diagram that our numerical results are in very good agreement with the theoretical prediction.

Finally, we fixed the peak position parameter x_0 to $x_0 = 25 \cdot 10^{-4}$m and the wavelength λ to $\lambda = 900$ nm and changed the value of the axicon's cone angle θ. We ran numerical simulations altering the value of θ from $\theta = 0.03°$ to $\theta = 0.48°$, multiplying its value by 2 each time, and we found the corresponding values of focus position f_{Ax}. In the following Table 4.6 we display our numerical results, compared to the corresponding theoretical prediction from equation (4.27).

Table 4.6

axicon's cone angle	theoretical prediction	numerical calculation	difference
$\theta(°)$	$f_{Ax}(m)$	$f_{Ax}(m)$	(%)
0.03	1.887	1.880	0.4
0.06	1.522	1.527	0.3
0.12	1.045	1.050	0.5
0.24	0.606	0.606	0.0
0.48	0.319	0.319	0.0

Furthermore, in Fig. 4.9, we have plotted in the same diagram the theoretical curve as predicted by (4.27) and the numerical results of the focus positions f_{Ax} as a function of the 1D axicon's cone angle θ.
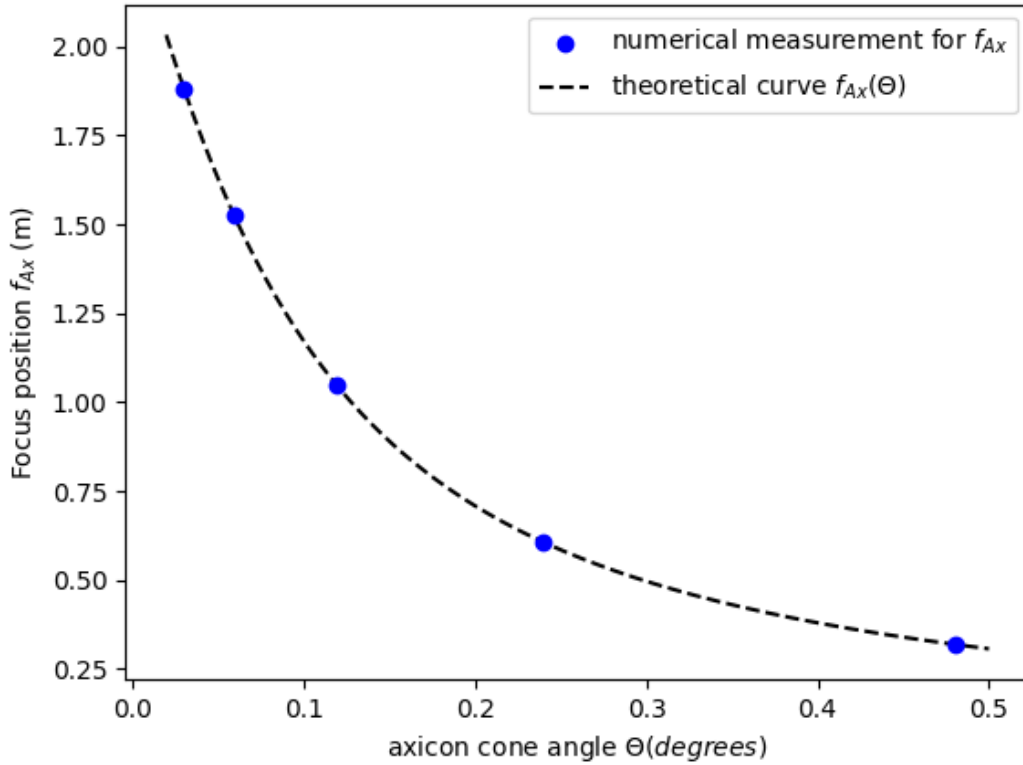

Figure 4.9: Focus position as a function of the 1D axicon cone angle θ.

Again, it is clear from the previous diagram that our numerical results are in very good agreement with the theoretical prediction, so we can conclude that the theoretical relation 3.11 has been numerically confirmed.

Appendix

In order to emphasize the analogy between wave optics and quantum mechanics, as revealed by the equivalency of equations (1.9) and (1.10), we conduct two numerical experiments. At the first one, we wish to see the intensity $I(x,z)$ of an optical beam with initial field distribution while propagating over $z - axis$:

$$u(x,0) = 3 \cdot e^{-(\frac{x-x_0}{d})^2} + 3 \cdot e^{-(\frac{x+x_0}{d})^2} \tag{4.28}$$

where $x_0 = 10^{-3}$ m, $d = 350\mu m$, $\lambda = 600$ nm, conducting a wave propagation simulation using $Wp - Maxima$. Then, we wish to see the time evolution of the probability density $P(x,t) = |\psi(x,t)|^2$ of an one-dimensional quantum-mechanical wavepacket with initial wavefunction:

$$\psi(x,0) = 3 \cdot e^{-(\frac{x-0.1}{0.35})^2} + 3 \cdot e^{-(\frac{x+0.1}{0.35})^2} \tag{4.29}$$

using the method of Exact Diagonalization in *Python*. We demonstrate the results of the simulations at the following Figure:
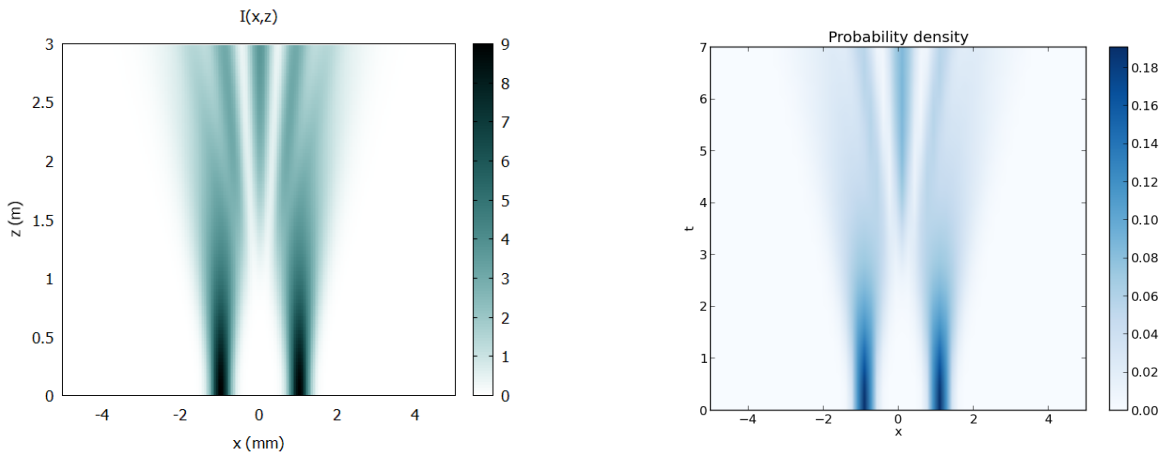
(a) Intensity image of optical beam's propagation over $z - axis(Wp - Maxima)$ [10]

(b) Probability density time evolution of wavepacket in one-dimensional chain (*Python*)

Figure 4.10: Comparison of the two different simulations

The similarity of the two images is totally evident, so the mathematical equivalence of the Eq.(1.8),(1.9) is confirmed in our numerical simulations.

Bibliography

[1] M. Born and E. Wolf, Principles of Optics: Electromagnetic Theory of Propagation, Interference and Diffraction of Light (7th Edition). Cambridge University Press, 1999.

[2] J. M. J. Durnin and J. H. Eberly, "*Diffraction-free beams*," Physical Review Letters, vol. 58, no. 15, pp. 1499–1501, 1987.

[3] J. Durnin, "*Exact solutions for nondiffracting beams I The scalar theory*," Journal of the Optical Society of America, vol. 4, no. 4, p. 651, 1987.

[4] M. V. Berry and N. L. Balazs, "*Nonspreading wavepackets*," Americal Journal of Physics, vol. 47, no. 3, pp. 264–267, 1979.

[5] O. Vallée and M. Soares, Airy Functions and Applications to Physics. IMPERIAL COLLEGE PRESS, sep 2004. [Online]. Available: http://www.worldscientific.com/worldscibooks/10.1142/p345

[6] G. A. Siviloglou and D. N. Christodoulides, "*Accelerating finite energy Airy beams*," Optics Letters, vol. 32, no. 8, p. 979, 2007.

[7] J. W. Goodman, Introduction to Fourier Optics, 2nd ed. New York: McGraw-Hill, 1996.

[8] M. Abramowitz and I. A. Stegun, Handbook of mathematical functions : with formulas, graphs, and mathematical tables. Dover Publications, 1970.

[9] D. G. Papazoglou, "Notes of postgraduate course: Wave optics and optical metrology," 2021.

[10] ——, "*wP*: An educational 1D+1 Virtual Lab wave propagation in *wxMaxima*," 2015.

[11] G. A. Siviloglou, J. Broky, A. Dogariu, and D. N. Christodoulides, "Observation of Accelerating Airy Beams," Physical Review Letters, vol. 99, no. 21, p. 213901, 2007. [Online]. Available: http://link.aps.org/abstract/PRL/v99/e213901http://dx.doi.org/10.1103/PhysRevLett.99.213901

[12] G. A. Siviloglou and D. N. Christodoulides, "Accelerating finite energy Airy beams," Opt. Lett., vol. 32, no. 8, pp. 979–981, 2007. [Online]. Available: http://ol.osa.org/abstract.cfm?URI=ol-32-8-979

[13] S. Wang and Q. Lin, "Non-diffraction properties of truncated Airy beams," Optik (Stuttg)., vol. 101, no. 2, pp. 47–, 1995.

[14] J. A. Anaya-Contreras, A. Zúñiga-Segundo, and H. M. Moya-Cessa, "Airy beam propagation: autofocusing, quasi-adiffractional propagation, and self-healing," J. Opt. Soc. Am. A, vol. 38, no. 5, p. 711, may 2021. [Online]. Available: https://www.osapublishing.org/abstract.cfm?URI=josaa-38-5-711

[15] N. K. Efremidis and D. N. Christodoulides, "*Abruptly autofocusing waves,*" Optics Letters, vol. 35, no. 23, p. 4045, 2010.

[16] J. Broky, G. A. Siviloglou, A. Dogariu, and D. N. Christodoulides, "Self-healing properties of optical Airy beams," Opt. Express, vol. 16, no. 17, p. 12880, aug 2008. [Online]. Available: http://www.opticsexpress.org/abstract.cfm?URI=oe-16-17-12880https://www.osapublishing.org/abstract.cfm?URI=oe-16-17-12880

[17] X. X. Chu, G. Q. Zhou, and R. P. Chen, "Analytical study of the self-healing property of Airy beams," Phys. Rev. A, vol. 85, no. 1, 2012.

[18] H. M. W. S. V. Garcés-Chávez, D. McGloin and K. Dholakia, "*Simultaneous micromanipulation in multiple planes using a self-reconstructing light beam,*" Nature, vol. 419, no. 6903, pp. 145–147, 2002.

[19] J. W. Z. Bouchal and M. Chlup, "*Self-reconstruction of a distorted nondiffracting beam,*" Optics Communications, vol. June, no. 151, pp. 207–211, 1998.

[20] A. D. John Broky, Georgios A. Siviloglou and D. N. Christodoulides, "*Self-Healing Properties of Airy Optical Beams*," Optics Express, vol. 16, no. 17, p. 12880, 2008.

[21] G. A. Siviloglou, J. Broky, A. Dogariu, and D. N. Christodoulides, "Ballistic dynamics of Airy beams," Opt. Lett., vol. 33, no. 3, pp. 207–209, 2008.

[22] D. G. Papazoglou, N. K. Efremidis, D. N. Christodoulides, and S. Tzortzakis, "Observation of abruptly autofocusing waves," Optics Letters, vol. 36, no. 10, pp. 1842–1844, 2011. [Online]. Available: http://ol.osa.org/abstract.cfm?URI=ol-36-10-1842

[23] I. Chremmos, N. K. Efremidis, and D. N. Christodoulides, "Pre-engineered abruptly autofocusing beams," Opt. Lett., vol. 36, no. 10, pp. 1890–1892, May 2011. [Online]. Available: http://ol.osa.org/abstract.cfm?URI=ol-36-10-1890

[24] D. G. Papazoglou, V. Y. Fedorov, and S. Tzortzakis, "Janus waves," Opt. Lett., vol. 41, no. 20, p. 4656, oct 2016. [Online]. Available: https://www.osapublishing.org/abstract.cfm?URI=ol-41-20-4656

[25] D. G. Papazoglou, "Notes on focusing of Janus waves," 2016.

[26] D. Mansour and D. G. Papazoglou, "Tailoring the focal region of abruptly autofocusing and autodefocusing ring-Airy beams," OSA Continuum, vol. 1, no. 1, p. 104, sep 2018. [Online]. Available: https://www.osapublishing.org/abstract.cfm?URI=osac-1-1-104